

LIGHT CURVE SIMULATION AND SHAPE INVERSION FOR HUMAN-MADE SPACE OBJECTS

by

Liam Robinson

A Thesis

Submitted to the Faculty of Purdue University

In Partial Fulfillment of the Requirements for the degree of

Master of Science in Aeronautics and Astronautics



School of Aeronautics and Astronautics

West Lafayette, Indiana

December 2023

**THE PURDUE UNIVERSITY GRADUATE SCHOOL
STATEMENT OF COMMITTEE APPROVAL**

Dr. Carolin Frueh

School of Aeronautics and Astronautics

Dr. Kenshiro Oguri

School of Aeronautics and Astronautics

Dr. Keith LeGrand

School of Aeronautics and Astronautics

Approved by:

Dr. Gregory Blaisdell

ACKNOWLEDGMENTS

This work was supported by Katalyst grant number FA6451-22-P-0019, Boeing work number SSOW-BRT-Z0722-5045, and the National Defense Science and Engineering Graduate Fellowship through the Air Force Office of Scientific Research under grant number FA9550-18-1-0154.

TABLE OF CONTENTS

LIST OF TABLES	9
LIST OF FIGURES	10
LIST OF SYMBOLS	12
ABSTRACT	13
1 Introduction	14
1.1 Problem Statement	14
1.2 State of the Art	15
1.3 Contributions	18
1.3.1 Simulation Advances	18
1.3.2 Advances in Convex Shape Inversion	18
1.3.3 Advances in Non-Convex Shape Inversion	19
2 Background	20
2.1 Coordinate Systems	20
2.1.1 Latitude, Longitude and Altitude	20
Altitude References	20
2.1.2 Topocentric Reference Frame	20
2.1.3 International Terrestrial Reference Frame (ITRF)	20
2.1.4 International Celestial Reference Frame (ICRF)	20
2.1.5 Right Ascension and Declination	20
2.1.6 Azimuth and Elevation	21
2.2 Time Systems	22
2.2.1 Time Scales	22
2.2.2 Julian Date	23
2.2.3 Solar and Sidereal Time	24
3 Attitude	25

3.1	Attitude Representations	25
3.1.1	The Direction Cosine Matrix	25
3.1.2	Principal Rotation Parameters	26
3.1.3	Quaternions	26
3.2	Quaternion Attitude Kinematics	27
3.3	Quaternion Attitude Dynamics	28
3.3.1	Analytic Attitude Propagation	28
4	Light Curves	29
4.1	Unresolved Imaging	29
4.1.1	The Light Curve	29
5	Photometry	30
5.1	Diffraction	30
5.1.1	Rayleigh Criterion	30
5.1.2	The Airy Disk	30
5.2	Astronomical Spectra	32
5.3	Brightness Units	33
5.3.1	Irradiance	33
5.3.2	Normalized Irradiance	34
5.3.3	S_{10}	34
5.3.4	Magnitude per Square Arcsecond	35
5.3.5	Candela	35
5.3.6	Photoelectron Counts	36
6	Background Model	38
6.1	Background Signal Sources	38
6.1.1	Background Source Importance	38
6.1.2	Airglow	39
6.1.3	Light Pollution	39
6.1.4	Twilight	41

6.1.5	Integrated Starlight	42
6.1.6	Scattered Moonlight	45
6.1.7	Zodiacal Light	47
6.1.8	Background Sampling	48
6.2	Sensor Effects	50
6.2.1	Dark Noise	50
6.2.2	Readout Noise	50
6.3	Signal to Noise Ratio (SNR)	50
6.4	Sampling Noisy Light Curves	50
7	Light Curve Simulation	51
7.1	Dynamics	51
7.1.1	Orbital Dynamics	51
	SGP4	51
7.2	Implicit and Explicit Shape Representations	51
7.3	The Wavefront OBJ File Format	51
7.4	Selected Satellite Models	52
7.5	The Bidirectional Reflectance Distribution Function	53
7.5.1	BRDF Formulations	55
	Lambertian	55
	Phong	55
	Blinn-Phong	56
	Glossy	56
	Cook-Torrance	56
	Oren-Nayar	56
	Ashikhmin-Shirley	57
	Summary	57
7.6	Simulating Convex Objects	57
7.7	Simulating Non-Convex Objects	58
7.7.1	The Importance of Self-Shadowing	58

7.7.2	Shadow Mapping	60
8	Light Curve Shape Inversion	62
8.1	Direct Convex Shape Inversion	62
8.1.1	The Extended Gaussian Image	62
8.1.2	EGI Optimization	63
8.1.3	EGI Resampling	65
8.1.4	EGI Merging	66
8.1.5	Geometry Recovery from the EGI	67
8.1.6	Support Vector Optimization	69
8.2	Non-Convex Feature Inversion	69
8.2.1	Non-Convex Feature Detection and Location	69
8.2.2	Concavity Creation	70
Model Subdivision	70	
Vertex Classification and Displacement	70	
8.3	Object Reconstruction Results	72
8.4	Shape Inversion With Noisy Measurements	73
9	Recommendations	75
10	Future Work	76
11	Appendices	77
11.1	Astronomical Spectra Data	77
Atmospheric Extinction	77	
Quantum Efficiency	78	
11.1.1	Background Source Data	79
Lunar Phase Factor	79	
Scattered Moonlight	79	
Zodiacal Light	80	
11.1.2	Telescope Parameters	81
Purdue Optical Ground Station	81	

11.1.3 File Formats	81
Wavefront OBJ Example	81
REFERENCES	83

LIST OF TABLES

6.1	Background signal importance	38
11.1	Purdue Optical Ground Station telescope parameters	81

LIST OF FIGURES

1.1	Public tracked catalog in 2000 and 2023	14
2.1	Time scales relative to TAI	23
5.1	Airy disk diffraction pattern	31
5.2	Astronomical Spectra from [42]	32
5.3	Luminous efficiency function from [44]	36
6.1	Airmass function comparison. The Van-Rhijn factor diverges to $+\infty$ while Pickering's function reaches the correct maximum of $AM(\theta_z) \approx 40$	40
6.2	Mean airglow signal on the local observer hemisphere. The observer is in New Mexico, USA at 32.900° N, -105.533° W	41
6.3	Zenith light pollution in the eastern USA, data from [46]	42
6.4	Mean light pollution signal on the local observer hemisphere. The observer is in New Mexico, USA at 32.900° N, -105.533° W	43
6.5	Twilight model surface brightness at zenith as a function of solar zenith angle .	44
6.6	Mean twilight signal on the local observer hemisphere. The observer is in New Mexico, USA at 32.900° N, -105.533° W	45
6.7	Raw image of three GEO objects with stars streaking through the background. As expected the star signals have a variety of signal-to-noise ratios. Taken by the Purdue Optical Ground station at 32.900° N, -105.533° W by Nathan Houtz. .	46
6.8	Integrated starlight brightness map	47
6.9	Integrated starlight signal on the local observer hemisphere. The observer is in New Mexico, USA at 32.900° N, -105.533° W	48
6.10	Mean scattered moonlight signal on the local observer hemisphere. The observer is in New Mexico, USA at 32.900° N, -105.533° W	49
6.11	Mean zodiacal light signal on the local observer hemisphere. The observer is in New Mexico, USA at 32.900° N, -105.533° W	50
7.1	Selected space objects with soccer field for size reference. In order, the objects are TESS, Starlink V1, TDRS, Landsat 8, Hispasat 30W-6, Saturn V SII, TELSTAR 19V, HYLAS 4, and simplified ASTRA.	53
7.2	Implemented BRDFs rendered with arbitrary parameters, demonstrating the qualitative differences between lighting models	57
7.3	Hubble Space Telescope ray traced shadow categorization and shading. Models from [58]	59

7.4	Brightness errors introduced by neglecting shadows for Bennu and HST. Models from [58]	59
7.5	Hubble Space Telescope shadow mapping with self (red) and horizon (blue) shadows rendered. Models from [58]	60
8.1	Simplified convex, non-convex, and open EGI nonuniqueness. Larger circles indicate greater relative areas assigned to a given normal vector.	63
8.2	Initial icosahedron EGI optimization before resampling	64
8.3	Resampled normal vectors (left) with reoptimized EGI (right)	66
8.4	Merged icosahedron EGI	67
8.5	Subdivided object (black) with reference (red) with various levels of subdivision	71
8.6	Root-adjacent and free vertices	72
8.7	Collapsed house, cube, icosahedron, and box-wing satellite reconstructions using vertex displacement	73
8.8	Convex objects under vertex displacement procedure	74

LIST OF SYMBOLS

I irradiance in $\left[\frac{W}{m^2}\right]$

\hat{I} normalized irradiance in $[W]$

ABSTRACT

Characterizing unknown space objects is an important component of robust space situational awareness. Estimating the shape of an object allows analysts to perform more accurate orbit propagation, probability of collision, and inference analysis about the object’s origin. Because most resident space objects of interest are unresolved when observed from the ground, state of the art techniques for object characterization often rely on the light curve – the time history of the object’s observed brightness. This problem is ill-posed without further assumptions; modern direct shape inversion methods require that the attitude profile of the object is known, or at least can be hypothesized. This work describes improvements to light curve simulation and direct shape inversion for non-convex and actively-controlled objects. In particular, this work finds that the proposed non-convex shape inversion method is effective at resolving large concave features, while a parametric approach performs well at fitting the geometry of active box wing satellites.

1. Introduction

1.1 Problem Statement

Humanity has been creating space debris since the dawn of the space age. Early missions like Vanguard 1 set a precedent by leaving both the satellite and the launch vehicle upper stage in orbit, of which are still in orbit in 2023 [1]. Half a century of increasingly frequent launches has created a space environment cluttered with thousands of debris objects, requiring active satellites in low Earth orbit (LEO) to perform regular avoidance maneuvers. This uncontrolled proliferation of human-made space debris puts space operations at risk. High-profile satellite collisions like Iridium-Cosmos in 2009 have added fuel to the fire, producing shells of debris that further pollute LEO [2]. Anti-satellite (ASAT) tests carried out by the USA, Russia, China, and India since the 1960s see nations destroying their own satellites, projecting military strength at the cost of creating more debris [2].

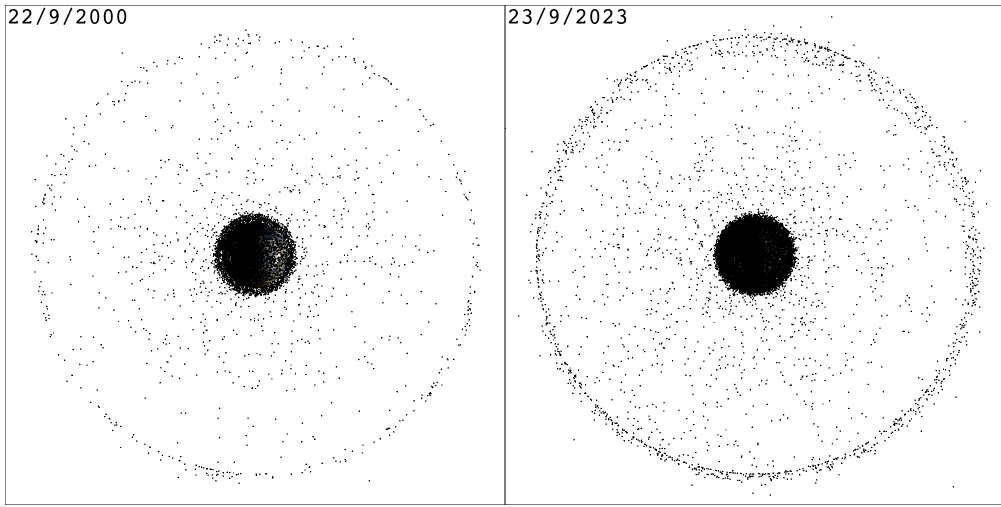


Figure 1.1. Public tracked catalog in 2000 and 2023

Determining the current state and predicting the future dynamics of space objects is critical for many fields within Space Domain Awareness (SDA) [3]. High-fidelity orbital propagation, collision avoidance, and fragmentation analysis all rely on accurate object characterization. Characterizing an object refers to estimating one or multiple unknown relevant properties. Estimating the shape of an object helps analysts characterize it, but doing so is difficult as distance and atmospheric turbulence prevents direct imaging [4]. As a result,

passive techniques for object characterization often rely on light curves – optical brightness measurements collected over time. Light curves are particularly efficient for the task as they are inexpensive to collect and contain information about the shape, orientation, and material properties of the object that produced them [4], [5]. Solving light curve inversion in a general case would enable robust active debris removal, anomaly detection, and collision avoidance, all of which rely on accurate shape information.

1.2 State of the Art

Light curve shape inversion was first investigated by Russell in 1906, who proposed a spherical harmonic shape representation that could be fit to an asteroid shape [6]. Russell was generally skeptical of the applicability of the method, hypothesizing that there would be ambiguity in the convex shape such that many solutions would fit the data equally well. After nearly a century of relative inactivity in the field, Kaasalainen and Torppa began successfully reconstructing the shapes of asteroids by directly optimizing the directions and areas of candidate faces to produce a convex shape that produces a similar light curve [7], [8]. Kaasalainen and Torppa also addressed non-convex shape inversion, developing an optimization procedure which performed well at reconstructed the largest nonconvex features [7]. The authors noted that this method was highly computationally demanding. The work of Kaasalainen and Torppa was extended by Durech and Kaasalainen in 2003, who investigated the observability of nonconvex features in asteroid light curves [9]. The authors noted that many nonconvex features are only observable at high phase angles, where self-shadowing effects become pronounced in the light curve. They further note that uncertainty in the surface optical properties generally means that small local features cannot be recovered through light curve inversion [9]. Using the methods originally proposed by Kaasalainen and Torppa, a collaborative effort between observatories lead to the publication of Database of Asteroid Models from Inversion Techniques (DAMIT), a publicly-available repository of convex asteroid models [10]. In 2022, Chng et al. investigated the

Papers in the literature usually propose methods for both light curve simulation and shape inversion. Often, the simulation method

Light curve simulation methods differ between approaches and the object class under study. Kaasalainen and Torppa employ a Lambertian model for convex objects with a facetwise ray tracing scheme for non-convex objects [8]. Fan, Friedman, Kobayashi, and Frueh use a nearly identical scheme for human-made objects [4], [11]–[14]. Allworth et al. developed a ray traced simulator for light curves in Blender, accounting for photorealistic shadowing and motion blur [15], [16]. Many deep learning approaches including Furfarro et al. [17] and Cabrera and Bradley [18], [19] use a simple Lambertian model with no self-shadowing. Linares and Crassidis apply a more specialized approach with a non-Lambertian Bidirectional Reflectance Distribution Function (BRDF) for lighting [20]. McNally et al. use a Phong BRDF without shadowing shadowing, citing computational intensity [21]. Blacketer implemented a Cook-Torrance BRDF for lighting with a plane stacking method for self-shadowing [22].

Methods for shape inversion fall into three major categories: Extended Gaussian Image (EGI), statistical estimation, and deep learning based methods, each approaching the problem from a different perspective.

Direct light curve inversion with the EGI uses a series of optimization problems to fit a convex shape to measurements. These methods were pioneered by Kaasalainen and Torppa for asteroids in [23] with simultaneous attitude inversion in [8]. The work of Kaasalainen et al. on asteroids was extended by Chng et al. to find globally optimal spin pole and area vector solutions [24]. Calef et al. were early adopters of Kaasalainen and Torppa’s EGI methods for human-made objects, focusing on multispectrum measurements [25]. Bradley and Axelrad applied EGI methods to recover convex approximations of representative GEO objects [19]. Fan and Frueh used the EGI with a multi-hypothesis scheme to recover human-made object shapes with measurement noise [4], [26], [27]. Friedman quantified the observability of EGI inversion to inform sensor tasking schemes [12], [28]. Cabrera et al. studied the effects of applying area regularization to Fan and Friedman’s methods to achieve more accurate reconstructions [18].

A second approach leverages statistical estimation to retrieve shape information. Linares et al. applied an unscented Kalman filter to estimate attitude and convex shape simultaneously, representing shape with vertex displacement on a sphere [29]. Linares et al. used

a Multiple-Model Adaptive Estimation (MMAE) algorithm to predict the truth geometry and attitude by comparing observations with a bank of reference objects [30]. Linares and Crassidis used an Adaptive Hamiltonian Markov Chain Monte Carlo scheme to estimate shape and other characteristics simultaneously [20].

A third approach for recovering shape information from light curves relies on deep learning. Linares and Furfaro used a deep convolutional neural network to classify novel light curves as rocket bodies, payloads, or debris [31]. Furfaro et al. used similar methods classify novel light curves into four truth object classes [17]. Kerr et al. adapted the architecture developed by Furfaro et al. to classify object shape and size in an extended training set [32]. McNally et al. investigated the use of different model training methods to identify satellites from simulated and real light curves [21]. Allworth et al. applied transfer learning to simulated and real measurements to classify object type [16].

Various unique methods have been applied to the light curve shape inversion problem. Hall et al. investigated methods for independently solving shape parameters in isolation without attitude information [33]. Fulcoly et al. used measurements from different sensor locations to determine shape under various attitude profiles [34]. Yanagisawa and Kurosaki fit an analytical light curve model for a tri-axial ellipsoid to derive the shape and attitude profile of a Cosmos rocket body [35]. Kobayashi used techniques from compressed sensing to recover shape information from light curves by taking advantage of shadowing geometry [13], [36].

Shape inversion for non-convex objects — mainly applied to asteroids — has been studied by others in the past. Durech and Kaasalainen [9] determined a relationship between concavity size and the minimum solar phase angle where self-shadowing impacts the light curve. Viikinkoski et al. [37] investigated recovering large concavities from adaptive optics imagery, noting the fundamental non-uniqueness of any solution. They discuss how a single large concavity may produce identical scattering behavior to multiple smaller concave features [37]. Cabrera et al. [18] studied convex solutions for non-convex objects, concluding that the convex fit diverges from the true shape as the relative concavity size increases.

TODO: complete this lit review, add new papers

1.3 Contributions

The framework detailed in this work contributes to the light curve simulation and shape inversion literature in a few notable areas.

1.3.1 Simulation Advances

A high-fidelity light curve simulator called LightCurveEngine was developed to support inversion algorithm development. Depending on the target shape, the simulator is one to four orders of magnitude faster than ray tracing-based renderers commonly used in literature [15], [26]. It supports self-shadowing, variable material properties, a variety of reflection functions, and dynamic solar panel rotation. In concert with a constrained observer model and orbit propagation, the engine generates realistic light curves for inactive debris, highly non-convex objects, and actively-controlled satellites.

1.3.2 Advances in Convex Shape Inversion

This work presents a suite of changes that build on the classical shape inversion algorithm for convex shapes [38]. New resampling and merging steps in the Extended Gaussian Image optimization stage yield more accurate shapes that are easier to reconstruct. An alternative optimization method for the shape support vector decreases convergence time for highly symmetric objects where the classical optimization algorithm fails.

The approach presented in this work solves the shape inversion problem beginning from the direct geometry reconstruction methods of [4], [8]. The EGI optimization processes of [4], [8], [18] are improved using novel resampling and merging steps. These improvements circumvent the need for the regularization terms explored by Cabrera et al. [18]. The support optimization procedure is accelerated and strengthened with a preconditioning term proposed by Nicolet et al. [39], enabling the rapid reconstruction of more detailed convex objects than previously feasible.

This convex shape inversion method has a number of general advantages. It does not require any *a priori* information about the truth geometry. Thus, unlike MMAE methods

[30], The presented algorithm does not require a bank of reference models to recover shape information. Unlike deep learning methods, the presented method does not rely on the diversity of a training set to achieve realistic results [17], [32].

1.3.3 Advances in Non-Convex Shape Inversion

While natural space objects like asteroids are largely convex, nearly all human-made space objects are highly non-convex, highlighting the need for a robust inversion scheme for both convex and non-convex space objects.

2. Background

2.1 Coordinate Systems

2.1.1 Latitude, Longitude and Altitude

Altitude References

TODO: ellipsoid, geoid, terrain

2.1.2 Topocentric Reference Frame

TODO: ENU here

2.1.3 International Terrestrial Reference Frame (ITRF)

The most intuitive class of Earth-centered reference frames is the Earth-centered Earth-fixed (ECEF) system. An ECEF frame has its origin at the center of mass of the Earth and its axes fixed in the crust. The fundamental plane of the frame is defined to be the equator — orienting the z -axis through Earth’s instantaneous spin axis, and the reference direction through the intersection of the prime meridian and the equator — defining the x -axis. Completing the right-handed system with $\hat{y} = \hat{z} \times \hat{x}$ yields a reference frame that remains fixed, neglecting effects like continental drift.

2.1.4 International Celestial Reference Frame (ICRF)

TODO

2.1.5 Right Ascension and Declination

Right ascension and declination, often shortened to RA/Dec, are useful angles from describing the angular position of an object on the celestial sphere from the perspective of an observer. Right ascension is defined as the angle of the observation projected onto the inertial $x - y$ plane, measured counterclockwise from inertial \hat{x} , represented by α . Declination is the angle from the $x - y$ plane to the observation with positive values above the $x - y$

plane (closer to inertial z) and negative values below. Declination is represented by δ . Given a unit vector direction $\hat{v} = [x, y, z]^T$ in inertial space, RA/Dec is computed via Eq 2.1 [3].

$$\begin{bmatrix} \alpha \\ \delta \end{bmatrix} = \begin{bmatrix} \text{atan2}(y, x) \\ \text{atan2}(z, \sqrt{x^2 + y^2}) \end{bmatrix} \quad (2.1)$$

TODO: add visual for the Az/El like Frueh notes fig 4.13

2.1.6 Azimuth and Elevation

Azimuth and elevation, often shortened to Az/El, are similar angular quantities to right ascension and declination [3]. Instead of being based on the inertial sphere, they are referenced to an arbitrary reference frame. For a telescope making observations of an object, the local East-North-Up (ENU) frame may be used. For a satellite star tracker, star azimuth and elevation might be reported in the satellite body frame. In either case, Eq 2.1 can be repurposed in terms of Az/El, where $\hat{v} = [x, y, z]^T$ is expressed in the frame of interest [3].

$$\begin{bmatrix} Az \\ El \end{bmatrix} = \begin{bmatrix} \text{atan2}(y, x) \\ \text{atan2}(z, \sqrt{x^2 + y^2}) \end{bmatrix} \quad (2.2)$$

Note that Eq 2.2 references azimuth to the x -axis, proceeding in the counterclockwise direction. Often, this reference axis and direction may be changed depending on the reference frame being used. For example, ground station observations may be referenced to local North — the second axis of the ENU system — proceeding clockwise. This would require the substitution $Az' = \frac{\pi}{2} - Az$. Notice that this substitution leads to Az' leaking outside the domain of $[0, 2\pi)$. This is not an issue for later coordinate transformations, but may be undesirable for plots. Wrapping the result back to the standard azimuth range via $Az_{wrapped} = \text{mod}(Az, 2\pi)$ is a sufficient fix.

2.2 Time Systems

2.2.1 Time Scales

There are a variety of scales used to measure time. What follows is a minimal treatment of each. For a more comprehensive overview, see Section 3.5 of [2]. International Atomic Time (TAI) is based on measurements from atomic clocks and is independent of astronomical effects or observations. By definition, TAI proceeds at the rate of 1 SI second per second. Universal Time (UT0) is derived directly from observations of the apparent position of the stars. UT1 is derived from UT0 by adjusting for polar motion. UT1 is offset from TAI by $\Delta UT1$, which is a dynamic quantity that must be continually observed. Universal Coordinated Time (UTC) is a truncation of UT1 that uses an integer number of leap seconds ΔAT to stay within 0.9 seconds of TAI. Terrestrial Time (TT) is defined by a constant offset of $TT - TAI = 32.184$ seconds from TAI and proceeding at the same rate as TAI. These time scale relations are summarized in Eq 2.3.

$$UTC = UT1 - \Delta UT1 \quad (2.3)$$

$$TAI = UTC + \Delta AT$$

$$TT = TAI + 32.184^s$$

These time scales are relevant for this research as the precise coordinate frame transformation from ITRF to the J2000.0 realization of ICRF relies on quantities expressed in UT1. Date timestamps are usually standardized to UTC, requiring the transformations in Eq 2.3 for full accuracy. Figure 2.1 shows the evolution of UTC, UT1, and TT with respect to TAI. Notice that $\Delta UT1$ continually changes while ΔAT is always truncated to a nearby integer.

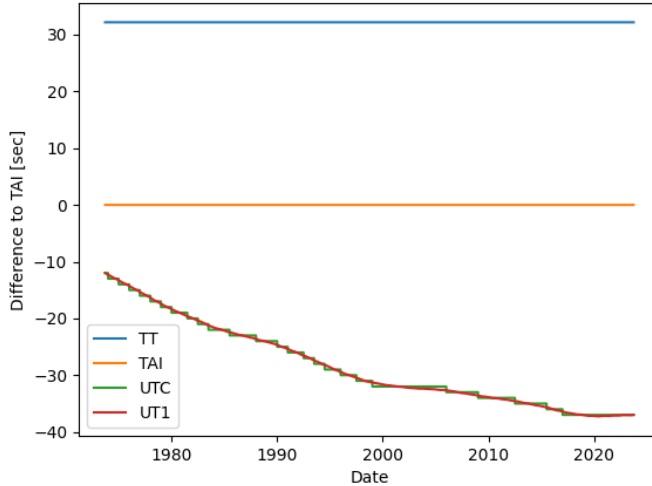


Figure 2.1. Time scales relative to TAI

2.2.2 Julian Date

Most tasks in astrodynamics are easier when using a continuous time system. For this reason, the Julian date is adopted. This quantity is defined as the number of days elapsed since January 1, 4713 B.C., at 12:00 [2]. Given a date timestamp of the form D/M/Y h:m:s between the years of 1900 and 2100, the Julian date is computed via Eq 2.4. Note that Eq 2.4 is always a function of the time scale used in the input, i.e., a UTC timestamp yields JD_{UTC} whereas a UT1 timestamp yields JD_{UT1} .

$$JD = 376Y - \text{floor} \left[\frac{7Y + 7 \cdot \text{floor} \left(\frac{M+9}{12} \right)}{4} \right] + \text{floor} \left(\frac{275M}{9} \right) + d + 1721013.5 + \frac{\frac{(s+60)}{60} + h}{24} \quad (2.4)$$

Another useful quantity for later time and coordinate system calculations is the number of Julian centuries since a particular epoch. The J2000.0 epoch is used unless otherwise stated, resulting in Eq 2.5 [2].

$$T = \frac{JD - 2451545.0}{36535} \quad (2.5)$$

Often, more specificity is needed with respect to the time scale used in Eq 2.5. For example, computing T with an input date in UT1 yields T_{UT1} using JD_{UT1} , which is in turn a function a date timestamp expressed in UT1.

2.2.3 Solar and Sidereal Time

A solar day is defined as the time required for the Sun to pass and return to an observer's meridian — a line of constant longitude extending from the geographic south pole to the geographic north pole [2]. By contrast, a sidereal day is the time required for the stars to complete a revolution around an observer's meridian. Due to the Earth's orbit around the Sun, the sidereal day is about 4 minutes shorter than the solar day [2]. The sidereal time is computed in seconds via

$$\theta_{GMST} = 67310.54841 + (3.15576e+09 + 8640184.812866)T_{UT1} + 0.093104T_{UT1}^2 - 6.2 \cdot 10^{-6}T_{UT1}^3. \quad (2.6)$$

3. Attitude

3.1 Attitude Representations

When discussing about the orientation of a rigid body in three dimensions, otherwise known as its attitude, that orientation is implicitly understood to be relative to some other reference frame. The direction of a unit vector can be expressed with two numbers — the azimuth and elevation of that vector. Naïvely, this could be extrapolated to conclude that six numbers are needed to express an orientation. Because the basis vectors form an orthonormal set $\{\hat{b}_1, \hat{b}_2, \hat{b}_3\}$, it follows for a right-handed system that $\hat{b}_3 = \hat{b}_1 \times \hat{b}_2$, $\hat{b}_2 = \hat{b}_3 \times \hat{b}_1$, and $\hat{b}_1 = \hat{b}_2 \times \hat{b}_3$. Each of these equations constrains one further degree of freedom, revealing that a minimum of three quantities are necessary to express the relative orientation of two reference frames. This minimum bound does not make any statements about the usefulness of three element sets; at least four dimensions are needed to remove singularities.

3.1.1 The Direction Cosine Matrix

The direction cosine matrix (DCM) is a 3×3 symmetric, orthogonal matrix, expressing the three basis vectors of one frame in another. This amounts to projecting each basis vector in the initial frame onto each basis vector of the final frame; the cosine of the angle between the compared vectors. It is notated with two capital letters, the rightmost indicating the reference frame of the input vectors and the leftmost indicating the transformed frame. Alternatively, the DCM is sometimes expressed as C when the frames involved are arbitrary or do not need to be denoted. For example, the DCM $[\mathcal{B}\mathcal{N}]$ takes vectors in the \mathcal{N} frame to the \mathcal{B} frame:

$${}^{\mathcal{B}}\mathbf{r} = [\mathcal{B}\mathcal{N}] {}^{\mathcal{N}}\mathbf{r} \quad (3.1)$$

The orthogonal property of the DCM implies $[\mathcal{B}\mathcal{N}]^{-1} = [\mathcal{B}\mathcal{N}]^T$ such that $[\mathcal{B}\mathcal{N}]^T = [\mathcal{N}\mathcal{B}]$.

3.1.2 Principal Rotation Parameters

Another common attitude representation is the Euler angle-axis set, otherwise known as principal rotation parameters [40]. Euler's rotation theorem guarantees that any relative orientation can be expressed as a single rotation about an axis $\hat{\lambda} \in \mathbb{S}^2$ by an angle $\theta \in [0, 2\pi]$ [40]. The set $\{\hat{\lambda}, \theta\}$ is known as a principal rotation parameter, abbreviated PRP hereafter. The DCM is mapped to the PRP representation via 3.2 [41].

$$\begin{aligned}\theta &= \cos^{-1} \left(\frac{1}{2} [C_{1,1} + C_{2,2} + C_{3,3} - 1] \right) \\ \hat{\lambda} &= \frac{1}{2 \sin \theta} \begin{bmatrix} C_{2,3} - C_{3,2} \\ C_{3,1} - C_{1,3} \\ C_{1,2} - C_{2,1} \end{bmatrix}\end{aligned}\tag{3.2}$$

Where $C_{i,j}$ refers to the i th row and j th column of C . The mapping from PRP to DCM is also relatively straightforward.

$$C = I_3 + \sin \theta [\hat{\lambda} \times] + (1 - \cos \theta) [\hat{\lambda} \times]^2\tag{3.3}$$

Where $[\mathbf{v} \times]$ is the matrix cross product operator, defined on $\mathbf{v} \in \mathbb{R}^3$ as:

$$[\mathbf{v} \times] = \begin{bmatrix} 0 & -v_3 & v_2 \\ v_3 & 0 & -v_1 \\ -v_2 & v_1 & 0 \end{bmatrix}.\tag{3.4}$$

This operator is useful as it rephrases the cross product as matrix multiplication, i.e. $\mathbf{v} \times \mathbf{u} = [\mathbf{v} \times] \mathbf{u}$. While the PRP $\{\theta, \hat{\lambda}\}$ is a four element set, there are only three degrees of freedom due to the unit norm constraint on $\hat{\lambda}$.

3.1.3 Quaternions

The quaternion represents attitude with a point on the surface of the hypersphere \mathbb{S}^3 . In terms of the PRP, the quaternion is given by Eq 3.5 [40].

$$\mathbf{q} = \begin{bmatrix} \hat{\lambda} \sin(\theta) \\ \cos(\theta) \end{bmatrix} \quad (3.5)$$

The first three entries of the quaternion are often called the vector component, with the final entry being the scalar component. Some authors reorder the quaternion, placing the scalar term first. Often the entries of a single quaternion are referenced by index such that $\mathbf{q} = [q_1, q_2, q_3, q_4]$. Similarly, the vector portion of the quaternion is referenced with $\mathbf{q}_{1:3}$. The quaternion can be mapped back to the PRP [40] via

$$\begin{aligned} \theta &= \cos^{-1}(q_4) \\ \lambda &= \frac{\mathbf{q}_{1:3}}{\sin \theta}. \end{aligned} \quad (3.6)$$

The quaternion maps to the DCM [40] via

$$C = \begin{bmatrix} -q_2^2 - q_3^2 + q_1^2 + q_4^2 & 2q_1q_2 + 2q_3q_4 & 2q_1q_3 - 2q_2q_4 \\ 2q_1q_2 - 2q_3q_4 & -q_1^2 - q_3^2 + q_2^2 + q_4^2 & 2q_1q_4 + 2q_2q_3 \\ 2q_1q_3 + 2q_2q_4 & 2q_2q_3 - 2q_1q_4 & -q_1^2 - q_2^2 + q_3^2 + q_4^2 \end{bmatrix} = \Xi(q)^T \Psi(q). \quad (3.7)$$

In Eq 3.7, Ψ is defined to be [40]

$$\Psi = \begin{bmatrix} q_4 & q_3 & -q_2 \\ -q_3 & q_4 & q_1 \\ q_2 & -q_1 & q_4 \\ -q_1 & -q_2 & -q_3 \end{bmatrix}. \quad (3.8)$$

3.2 Quaternion Attitude Kinematics

Because it is cheap to convert between attitude representations, only one set of kinematic equations are needed for propagating a rigid body attitude profile from an initial con-

dition. Quaternion kinematic differential equations are chosen as they have no singularity and produce very smooth dynamics that are easy to integrate when compared to three-variable representations that possess singularities. Given the current orientation quaternion $\mathbf{q} = [q_1, q_2, q_3, q_4]^T$ and angular velocity $\omega = [\omega_1, \omega_2, \omega_3]^T$ the quaternion derivative is computed via Eq 3.9

$$\begin{bmatrix} \dot{\epsilon}_1 \\ \dot{\epsilon}_2 \\ \dot{\epsilon}_3 \\ \dot{\epsilon}_4 \end{bmatrix} = \frac{1}{2} \begin{bmatrix} \epsilon_4 & -\epsilon_3 & \epsilon_2 & \epsilon_1 \\ \epsilon_3 & \epsilon_4 & -\epsilon_1 & \epsilon_2 \\ -\epsilon_2 & \epsilon_1 & \epsilon_4 & \epsilon_3 \\ -\epsilon_1 & -\epsilon_2 & -\epsilon_3 & \epsilon_4 \end{bmatrix} \begin{bmatrix} \omega_1 \\ \omega_2 \\ \omega_3 \\ 0 \end{bmatrix}. \quad (3.9)$$

3.3 Quaternion Attitude Dynamics

Rigid body dynamics can be easily expressed in the body principal axes with an arbitrary torque $\mathbf{M} = [M_1, M_2, M_3]^T$ in the same frame via Eq 3.10

$$\begin{bmatrix} \dot{\omega}_1 \\ \dot{\omega}_2 \\ \dot{\omega}_3 \end{bmatrix} = \begin{bmatrix} (M_1 + I_2\omega_2\omega_3 - I_3\omega_2\omega_3) / I_1 \\ (M_2 - I_1\omega_1\omega_3 + I_3\omega_1\omega_3) / I_2 \\ (M_3 + I_1\omega_1\omega_2 - I_2\omega_1\omega_2) / I_3 \end{bmatrix} \quad (3.10)$$

3.3.1 Analytic Attitude Propagation

TODO: single axis solution, axisymmetric solution

4. Light Curves

4.1 Unresolved Imaging

TODO: add SNR reduction on CCD image, discuss what it means to be unresolved

4.1.1 The Light Curve

A light curve is a time series of unresolved optical brightness measurements. Once an object is far enough away from the observer to become unresolved, all geometric data is lost and the only information that remains in the individual measurements is the total brightness.

5. Photometry

5.1 Diffraction

5.1.1 Rayleigh Criterion

Many objects of interest are far past low-Earth orbit, making optical observations diffraction limited. Diffraction is always occurring when observing an object at any distance through any optics, but it begins to dominate when the object's scale is equal or smaller than the Rayleigh criterion. The Rayleigh criterion states that light of wavelength λ will spread into a diffraction pattern with the first minimum of the distribution at an angular radius θ_R when passing through a circular aperture of diameter d such that:

$$\sin \theta_R = 1.22 \frac{\lambda}{d}. \quad (5.1)$$

For a 1-meter aperture optical telescope observing a 10-meter diameter object in GEO – giving an angular radius of $\approx 10^{-7}$ radians – Eq 5.1 predicts that the diffraction pattern will be 5 times wider than the object. As a result, GEO objects cannot be resolved from the ground, independent of atmospheric effects.

5.1.2 The Airy Disk

The far-field diffraction pattern produced by a point source is known as an Airy pattern [3]. The Airy disk is expressed in terms of an amplitude C at an angular distance θ from the center $C(\theta)$ as:

$$C_{\text{Airy}}(\theta) = C_0 \left(\frac{2J_1(k \cdot r_d \sin \theta)}{k \cdot r_d \sin \theta} \right). \quad (5.2)$$

In Eq 5.2, C_0 is the amplitude of the center of the Airy disk, r_d is the radius of the aperture, $k = \frac{2\pi}{\lambda}$ is the wavenumber, and J_1 is the first order Bessel function of the first kind. The central magnitude C_0 is expressed:

$$C_0 = \frac{\bar{C}_{\text{all}}^2 D^2}{2f^4}. \quad (5.3)$$

In Eq 5.3, \bar{C}_{all} is the total mean signal incident on the CCD due to the source, D is the aperture area, and f is the focal length of the optics [3]. The pattern produced by Eq 5.2 is depicted in Figure 5.1.

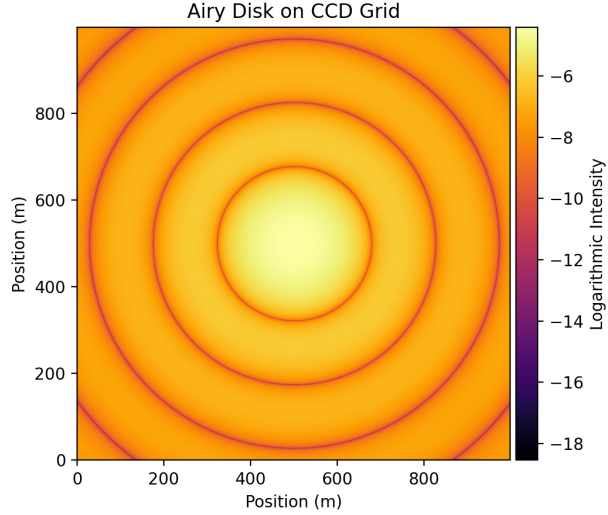


Figure 5.1. Airy disk diffraction pattern

The Rayleigh criterion expresses the angular size of the first zero of the Airy disk, after which the amplitude of the Airy disk drops off exponentially. It is often useful to approximate the Airy disk with a 2D Gaussian. We can fit this Gaussian with a single parameter – the full width at half maximum (FWHM). The FWHM expresses the diameter at which the signal drops to half the magnitude of its central maximum [3]. The FWHM of the Airy disk is expressed:

$$FWHM_{\text{airy}} = \frac{1.028\lambda}{2r_d}. \quad (5.4)$$

The diffraction pattern is not the only effect that spreads the unresolved signal over the pixel grid. Atmospheric turbulence contributes to further spreading and speckling of the signal [3]. This effect – known as the *seeing* – is encapsulated in $FWHM_{\text{seeing}}$ and is generally between 1 and 3 arcseconds [3]. While the seeing and diffraction pattern are additive, it is sufficient to take the larger value for simulation purposes [3]. The standard deviation of the Gaussian approximation of the Airy disk is given by:

$$\sigma = \frac{FWHM}{2\sqrt{2 \ln 2}}. \quad (5.5)$$

The full Gaussian approximation at an angular distance θ from the source is given by:

$$C_{Gauss}(\theta) = \frac{0.838\bar{C}_{all}}{2\pi\sigma^2} \exp\left(-\frac{\theta}{2\sigma^2}\right) \quad (5.6)$$

In practice, computing the Airy disk or its Gaussian approximation on rectangular pixel grid amounts to integrating the amplitude function $C(\theta)$ over the pixel area:

$$C_{pix}(x, y) = \int_x^{x+\Delta x} \int_y^{y+\Delta y} C(\theta) dy dy. \quad (5.7)$$

5.2 Astronomical Spectra

Four of the quantities needed for the background model vary with wavelength. These are the atmospheric transmission, the sensor quantum efficiency, the irradiance of a 0th magnitude star, and the solar spectrum. Each spectrum is displayed in Figure 5.2.

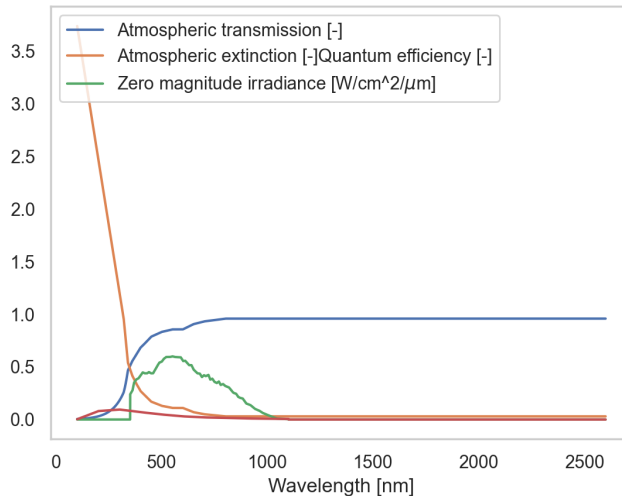


Figure 5.2. Astronomical Spectra from [42]

In practice, the quantum efficiency curve varies by sensor and the thermal conditions of the observation. The curve adopted in this work is that used by Krag; modern sensors will often perform better.

5.3 Brightness Units

In the context of photometry, "brightness" is a catch-all term for a variety of units. Let's explore the relationships between these units to make later conversions more clear.

5.3.1 Irradiance

Irradiance is the standard SI linear unit used to describe the total amount of energy incident on a surface from a given source. An irradiance of $1 \left[\frac{W}{m^2} \right]$ implies that a $10 [m]$ area would experience $10 [W]$ of incident power. The Sun's irradiance at a distance of 1 AU is known as the solar constant and is approximately $1361 \left[\frac{W}{m^2} \right]$.

Visual magnitude — also known as apparent or relative magnitude — is a reverse logarithmic scale that originates in astronomy [3]. Stellar sources span many orders of magnitude of brightness, making a logarithmic scale a helpful middle ground for comparison. Note that apparent magnitude always expresses brightness at the observer's location; absolute magnitude is a different quantity that normalizes brightness from a distance of 10 parsecs [3]. Apparent magnitude m is computed from irradiance via Eq 5.8.

$$m = -2.5 \log_{10} \left(\frac{I}{I_0} \right) \quad (5.8)$$

In Eq 5.8, I is the irradiance of the source of interest and I_0 is irradiance of the zero-point source. This makes sense; substituting $I = I_0$ returns $m = 0$. The star Vega is usually taken to be the zero-point with irradiance $I_0 = 2.518021002 \cdot 10^{-8} \left[\frac{W}{m^2} \right]$ [3].

We can rearrange Eq 5.8 to compute irradiance from a given apparent magnitude, yielding Eq 5.9.

$$I = I_0 \cdot 10^{-\frac{m}{2.5}} \quad (5.9)$$

5.3.2 Normalized Irradiance

The light curve simulation methods presented in this work heavily use normalized irradiance, the irradiance of a source observed from a distance of 1 meter. This is a non-standard quantity in the literature, but proves useful for the same reasons absolute magnitude is used by astronomers. Adjusting sources to be at a standard distance allows us to simulate and invert light curves in a non-dimensionalized space. This simplifies simulation and makes the shape inversion optimizations more robust. To make the conversion explicit, irradiance observed at a distance r in meters from an object is converted to normalized irradiance \hat{I} in watts via Eq 5.10.

$$\hat{I} = r^2 I \quad (5.10)$$

5.3.3 S_{10}

While apparent magnitude and irradiance are effective for quantifying the flux of point sources, other units exist to describe diffuse or extended sources where brightness is spread over an area. S_{10} is a unit of surface brightness representing the number of 10th magnitude stars per square degree that would produce the same flux as a given diffuse source. Surface brightness in S_{10} over a given solid angle Ω [sr] can be converted to total irradiance I [$\frac{W}{m^2}$] via Eq 5.11.

$$\frac{I \left[\frac{W}{m^2} \right]}{S_{10}} = 10^{-10/2.5} \left(\Omega \frac{180^2}{\pi^2} \right) \int_{10^{-8}}^{10^{-6}} \text{STRINT}(\lambda) d\lambda = 8.26617 \Omega \cdot 10^{-9} \quad (5.11)$$

In 5.11, $\text{STRINT}(\lambda) \left[\frac{W}{m^2 \cdot m} \right]$ is the representative spectrum of a 0th magnitude star, $\text{QE}(\lambda)$ is the quantum efficiency spectrum of the observing sensor, $\text{ATM}(\lambda)$ is the atmospheric transmission spectrum, $\lambda [m]$ is wavelength, $h \left[\frac{m^2 \cdot kg}{s} \right]$ is Plank's constant, and $c \left[\frac{m}{s^2} \right]$ is the speed of light in vacuum. Quantum efficiency has units of photoelectrons which conveys the fraction of incident photons which are (proportionally) converted to photoelectrons in the CCD sensor. Atmospheric transmission is a unitless quantity conveying the fraction of

light that is not absorbed by the atmosphere. Example spectra for $\text{ATM}(\lambda)$ and $\text{QE}(\lambda)$ are displayed in Figure 5.2, with underlying data provided in Appendices 11.1 and 11.1.

5.3.4 Magnitude per Square Arcsecond

A second surface brightness unit is $\left[\frac{\text{mag}}{\text{arcsec}^2}\right]$, also known as MPSAS (magnitude per square arcsecond). This quantity can be thought of as a generalized S_{10} , where instead of quantifying the number of stars of a certain magnitude in a solid angle, the equivalent magnitude of a single point source is measured. A surface brightness B_{10} in S_{10} can be converted into surface brightness B_{mag} in $\left[\frac{\text{mag}}{\text{arcsec}^2}\right]$ via Eq 5.12.

$$B_{\text{mag}} = -2.5 \log_{10} \left(\frac{B_{10} \cdot 10^{-4}}{12960000} \right) \quad (5.12)$$

In Eq 5.12 S_{10} is first converted to the total irradiance per square degree, convert square degrees to square arcseconds, and transform the result back into apparent magnitude. MPSAS is converted to irradiance per steradian via Eq 5.13 using 5.9.

$$I = \left(\frac{180}{3600\pi} \right)^2 I_0 \cdot 10^{-\frac{\text{MPSAS}}{2.5}} \quad (5.13)$$

5.3.5 Candela

Some light pollution datasets are given in units that include candela. Candela is the SI base unit of luminous intensity defined by the International Committee for Weights and Measures as "Fixing the numerical value of the luminous efficacy of monochromatic radiation of frequency $540 \cdot 10^{12}$ Hz to be equal to exactly 683" [43]. This means that an isotropic green light source with frequency $540 \cdot 10^{12}$ Hz ($\lambda = 555$ nm) has a luminous efficacy of $K_{cd} = 683$ [lm/W] where lm stands for lumens. Luminous efficacy itself determines how well a source produces visible light. For a given wavelength, candela B_{cd} is converted to watts per steradian B_{wsr} via Eq 5.14 [43]

$$B_{wsr}(\lambda) = \frac{B_{cd}}{K_{cd}(\lambda)}. \quad (5.14)$$

The luminous efficiency function $K_{cd}(\lambda)$ models the human eye's response to the visible spectrum [44]. Different fits of this function exist; the function proposed Sharpe et al. is adopted, displayed in Figure 5.3 [44].

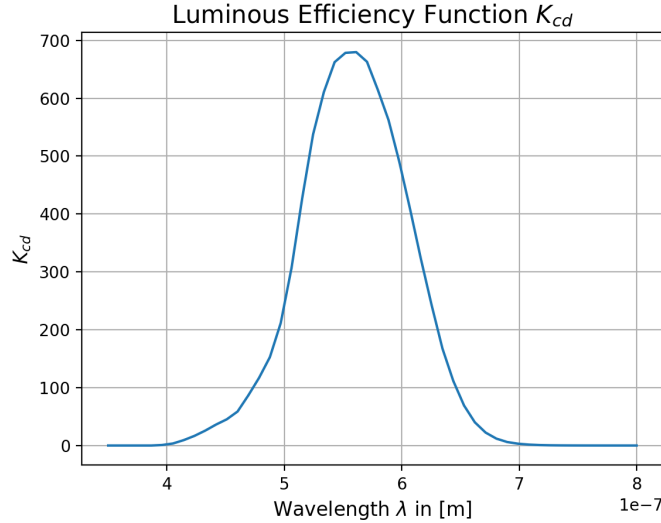


Figure 5.3. Luminous efficiency function from [44]

Candela per unit area can be converted into MPSAS by combining Eq 5.14 with 5.8, yielding Eq 5.15, which is still a function of the source's wavelength.

$$MPSAS(\lambda) = -2.5 \log_{10} \left(\frac{B_{cd}}{\left(\frac{180}{3600\pi} \right)^2 K_{cd}(\lambda) I_0} \right) \quad (5.15)$$

5.3.6 Photoelectron Counts

Raw images taken by a CCD-equipped telescope have pixel values measured in photo-electron counts, otherwise known as Analog-to-Digital Units (ADU) [42]. The count in a single pixel obtained is directly proportional (via the CCD's gain) to the number of photons incident on that pixel during the integration time. Higher order effects in the silicon of the CCD makes this description incomplete, but for non-resolved imaging applications concerned about, effects smaller than the sensor readout noise and dark current can be safely neglected [3]. Irradiance can be converted to ADU via the conversion factor $SINT$ in Eq 5.16 [42].

$$\text{SINT} = \frac{\pi D^2}{4} \int_{10^{-8}}^{10^{-6}} \left(\frac{\text{SUN}(\lambda)}{I_{\text{sun}}} \right) \cdot \text{QE}(\lambda) \cdot \text{ATM}(\lambda) \cdot \left(\frac{\lambda}{hc} \right) d\lambda \quad (5.16)$$

In Eq 5.16, $\text{SUN}(\lambda)$ is the spectrum of solar irradiance in $\left[\frac{W}{m^2 \cdot m} \right]$, I_{sun} is the irradiance of the Sun (generally taken to be the solar constant 1361 $\left[\frac{W}{m^2} \right]$). Read literally, the integral term as units $\left[\frac{1}{W_s} \right]$, giving the number of counts per incident Watt of solar radiation and second of integration time. The aperture diameter factor outside the imintegral accounts for the area of light incident on the CCD, giving SINT units of $\left[\frac{m^2}{W_s} \right]$. The spectra in Eq 5.16 are plotted in Figure 5.2 with data in Appendix 11.1. Multiplying by irradiance in $\left[\frac{W}{m^2} \right]$ and an integration time Δt in seconds will yield the count of photoelectrons S in ADU as shown in Eq 5.17.

$$S = \text{SINT} \cdot I \cdot \Delta t \quad (5.17)$$

For completeness, irradiance can be recovered from a signal in ADU and the integration time via Eq 5.18.

$$I = \frac{S}{\text{SINT} \cdot \Delta t} \quad (5.18)$$

6. Background Model

Whenever an optical telescope is observing an unresolved space object, the object's signal is necessarily superimposed on whatever signals exist in the background as the unresolved signal spreads much further than the object's actual geometric bounds. In this context, background does not only refer to sources physically further than the object — as light can easily enter optical path through atmospheric scattering — but all sources that impact the image apart from the object signal. Some of these sources even originate within the telescope optics and its sensor. To faithfully simulate a telescope observing an object, many position-based SDA tasks are able to ignore background effects while acquiring or tracking objects. For photometry-based SDA, the background is critical. The overall noise floor can be broken up into background signal sources and sensor effects.

6.1 Background Signal Sources

6.1.1 Background Source Importance

Some background signals are more impactful than others. Table 6.1 details the approximate magnitudes in photoelectrons per pixel one can expect from a telescope similar to the Purdue Optical Ground Station.

Source	Magnitude [e^-/pix]
Airglow	$10^3 - 10^4$
Scattered moonlight	$0 - 10^5$
Integrated starlight	$10^1 - 10^2$
Light pollution	$10^2 - 10^3$
Zodiacal light	$10^2 - 10^4$
Twilight	$10^1 - 10^7$

Table 6.1. Background signal importance

6.1.2 Airglow

Certain chemical reactions from 80-110 km altitude in the upper atmosphere release visible light [42]. This effect is known as airglow. Since these reactions are assumed to be isotropic — equally intense when integrated along any vertical line extending upwards from the surface. The airglow signal AINT is modeled in a similar fashion to integrated starlight. Given the airglow spectra GLINT(λ) $\left[\frac{W}{m^2 \cdot m \cdot sr}\right]$, the airglow signal is computed via Eq 6.1 [42].

$$\text{AINT} = \frac{\pi D^2}{4} \int_{10^{-8}}^{10^{-6}} \text{GLINT}(\lambda) \cdot \text{QE}(\lambda) \cdot \text{ATM}(\lambda) \cdot \left(\frac{\lambda}{hc} \right) d\lambda \quad (6.1)$$

The quantity AINT has units $\left[\frac{1}{s \cdot sr}\right]$, meaning that the mean airglow signal in ADU per pixel is simply given by Eq 6.2

$$\bar{S}_{\text{airglow}} = \text{AINT} \cdot \text{AM}(\theta_z) \cdot \Delta t \cdot \left(\frac{\pi s_{\text{pix}}}{648000} \right)^2 \quad (6.2)$$

In Eq 6.2, $\text{AM}(\theta_z)$ is the relative airmass function which accounts for the accumulation of air along the optical path at different zenith angles [3]. This airmass is termed *relative* as it relates the ratio of absolute airmass at a zenith angle to the absolute airmass at zenith. Often, this function is approximated by the Van-Rhijn factor $\text{AM}(\theta_z) = \sec \theta_z$ which remains accurate up to $\theta_z \approx 70^\circ$ before diverging to infinity. Instead, a function proposed by Pickering is used [45].

$$\text{AM}(\theta_z) = \frac{1}{\sin \left((90 - \theta_z) + \frac{244}{165 + 47 * (90 - \theta_z)^{1.1}} \right)} \quad (6.3)$$

Using Eq 6.3 instead of the Van-Rhijn factor is important for computing background signals near the horizon. Figure 6.1 displays this comparison in action.

6.1.3 Light Pollution

Another source of background noise light pollution. On a cloudless night with low levels of atmospheric aerosols, the zenith surface brightness is approximately $22 \left[\frac{\text{mag}}{\text{arcsec}^2} \right]$ (MPSAS)

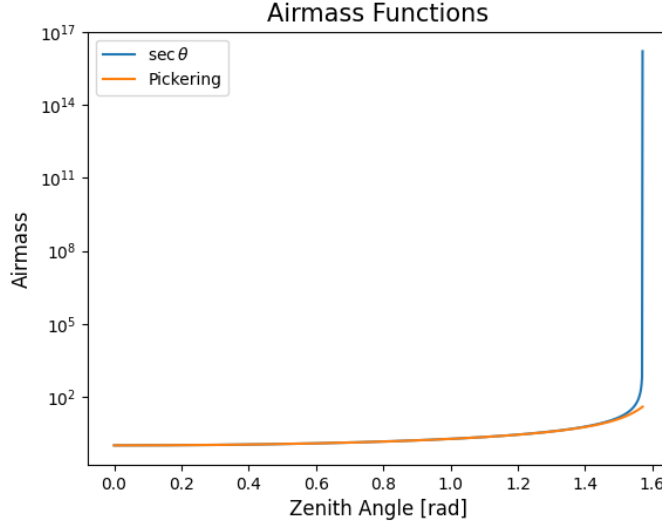


Figure 6.1. Airmass function comparison. The Van-Rhijn factor diverges to $+\infty$ while Pickering’s function reaches the correct maximum of $\text{AM}(\theta_z) \approx 40$.

[42]. As light pollution increases, this zenith brightness may dip down to $14 - 15 \left[\frac{\text{mag}}{\text{arcsec}^2} \right]$. To get accurate localized zenith brightness values, we use the 2015 World Atlas of Sky Brightness dataset [46]. The data is reported in $\left[\frac{\text{mcd}}{\text{cm}^2} \right]$ on a 30-arcsecond grid, requiring conversion to a more useful unit. A subset of the global dataset is displayed in 6.3 This conversion is listed in Eq 5.15, using a monochromatic $\lambda = 474 \text{ nm}$ to fit Falchi et al.’s example conversions [47].

The mean light pollution CCD signal in ADU per pixel is formulated similarly to airglow. The station’s zenith surface brightness $B_{poll,z}$ in MPSAS, linearly interpolated from the World Atlas dataset, is converted to irradiance per steradian via 5.13 and to ADU per pixel via 6.4. Note that Krag does not implement a specific light pollution model, but instead takes the dark sky site zenith brightness of 22 MPSAS as input to an atmospherically scattered light model. This is simply an adaptation of Krag’s model with a variable zenith brightness.

$$\bar{S}_{pollution} = B_{poll,z} \cdot SINT \cdot \text{AM}(\theta_z) \cdot \Delta t \cdot \left(\frac{\pi s_{pix}}{648000} \right)^2 \quad (6.4)$$

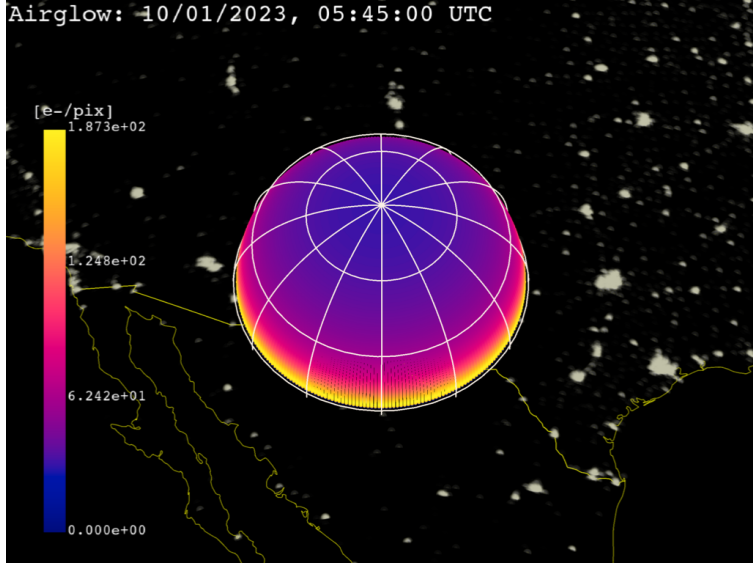


Figure 6.2. Mean airglow signal on the local observer hemisphere. The observer is in New Mexico, USA at 32.900° N, -105.533° W

6.1.4 Twilight

Even after the Sun sets, scattered sunlight in the upper atmosphere creates a signal on our CCD. The twilight model implemented for this work is due to Patat et al. and was developed for the European Southern Observatory at Paranal in Chile [48]. This model implements the zenith brightness as a function of the solar zenith angle γ — the angle from zenith to the Sun’s apparent centroid. Patat et al.’s model fits a second-degree polynomial in γ to approximately 2000 observations in varying atmospheric conditions, yielding separate curves for each of the UBVRI passbands. For example, for the V band, the twilight zenith brightness in MPSAS is given by 6.5 [48].

$$B_{twi,z} = 11.84 + 1.518(\gamma - 95^{\circ}) - 0.057(\gamma - 95^{\circ})^2 \quad (6.5)$$

Eq 6.5 is valid from $95^{\circ} \leq \gamma \leq 105^{\circ}$. While $\gamma \leq 95^{\circ}$, the zenith brightness is taken to be constant and equal to the brightness at $\gamma = 95^{\circ}$. This is not accurate, as it predicts daylight to be the brightness of twilight, but is sufficiently bright to correctly forbid daytime observations by lowering the SNR drastically. After $\gamma = 105^{\circ}$ the zenith surface brightness is

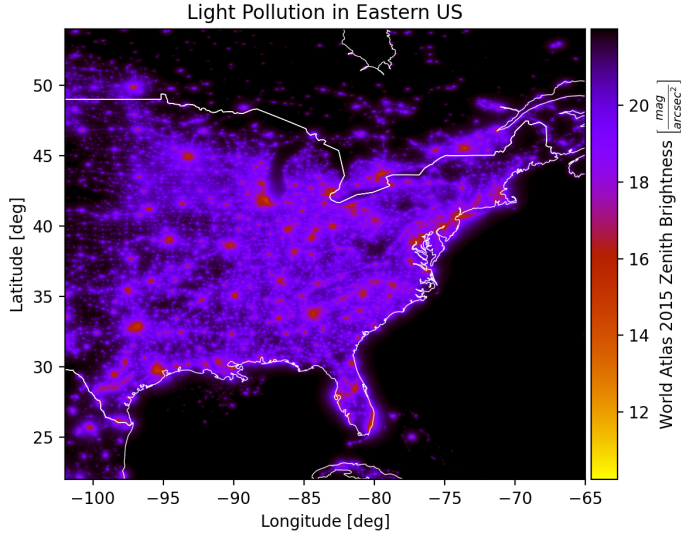


Figure 6.3. Zenith light pollution in the eastern USA, data from [46]

set to $B_{twi,z} = 22$ MPSAS to match the optimal observation condition of the light pollution model [42]. Zenith twilight brightness is plotted as a function of γ in Figure 6.5.

Computing the mean CCD signal in ADU per pixel due to the twilight brightness proceeds identically to the light pollution formulation.

$$\bar{S}_{twilight} = B_{twi,z} \cdot SINT \cdot AM(\theta_z) \cdot \Delta t \cdot \left(\frac{\pi s_{pix}}{648000} \right)^2 \quad (6.6)$$

6.1.5 Integrated Starlight

Stars are almost always present in optical images of space objects. The brightest stars streaking across the field of view in Figure 6.7 have high SNRs and stand out clearly against the dark background. This raises a question: if the telescope observes a full $1^\circ \times 1^\circ$ area of the sky, where are the rest of the stars? The Milky Way alone contains approximately $1 \cdot 10^{11}$ stars. The answer is clear: many more stars are present in the image, most of them falling into the background. This residual faint starlight is called "integrated" starlight.

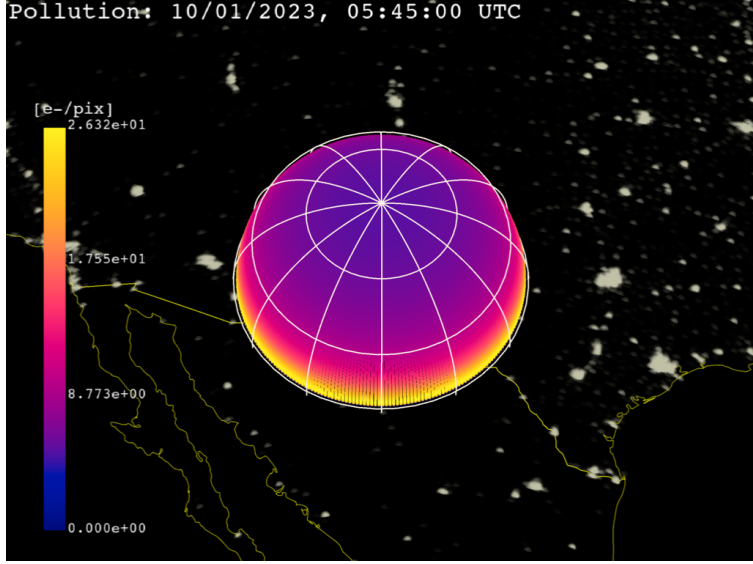


Figure 6.4. Mean light pollution signal on the local observer hemisphere. The observer is in New Mexico, USA at 32.900° N, -105.533° W

Krag [42] modeled this signal by building a $1^{\circ} \times 1^{\circ}$ grid of surface brightness values for the full inertial sphere, parameterized by RA/Dec. Krag used the Guide Star catalog, which contains 15 million stars down to apparent magnitude 16. Exponential extrapolation was used to predict star counts in each bin for higher magnitudes [42]. Twenty years later, larger star catalogs exist that are nearly complete to much higher apparent magnitudes. The integrated starlight catalog used in this work was built from the GAIA catalog with approximately 1.5 billion stars down to magnitude 21-22 [49]. The same $1^{\circ} \times 1^{\circ}$ grid was computed using the `astroquery.gaia` Python package [50]. Figure 6.8 shows the computed brightness map, in units of S_{10} .

With this map of exoatmospheric mean brightness of the night sky due to integrated starlight, the corresponding signal mean in the telescope CCD is computed, adopting Krag's formulation [42].

$$\text{BINT} = \frac{\pi D^2}{4} \int_{10^{-8}}^{10^{-6}} \text{STRINT}(\lambda) \cdot \text{QE}(\lambda) \cdot \text{ATM}(\lambda) \cdot \left(\frac{\lambda}{hc} \right) d\lambda \quad (6.7)$$

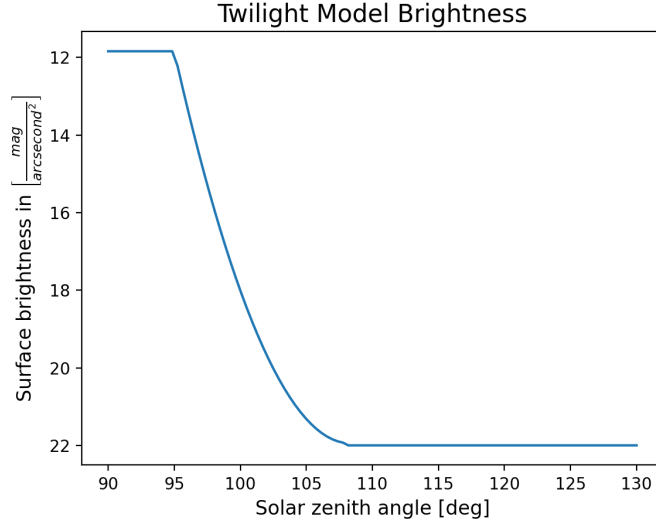


Figure 6.5. Twilight model surface brightness at zenith as a function of solar zenith angle

In Eq 6.7, D is the telescope aperture diameter in meters, h is Plank's constant in $\left[\frac{m^2 kg}{s}\right]$, and c is the speed of light in vacuum in $\left[\frac{m}{s}\right]$. The resulting quantity BINT has units of $\left[\frac{1}{s}\right]$, representing the mean total photons passing through the telescope aperture due to integrated starlight.

$$\bar{S}_{star} = 10^{-4} \cdot BINT \cdot \left(\frac{s_{pix}}{3600}\right)^2 \cdot \Delta t \cdot b_{is} \quad (6.8)$$

In Eq 6.8, b_{is} is the integrated starlight brightness in $[S_{10}]$ computed by linearly interpolating the dataset in Figure ??, s_{pix} is the telescope pixel scale in $\left[\frac{\text{arcsecond}}{\text{pix}}\right]$, and Δt is the integration time in seconds. Note the addition of the 10^{-4} factor to reconcile catalog surface brightness in terms of 10th magnitude stars, and the 0th magnitude source in BINT. This yields \bar{S}_{star} with units $\left[\frac{e^-}{\text{pix}^2}\right]$; photoelectron counts (ADU) per pixel. Figure 6.9 shows the background signal mean due to integrated starlight.

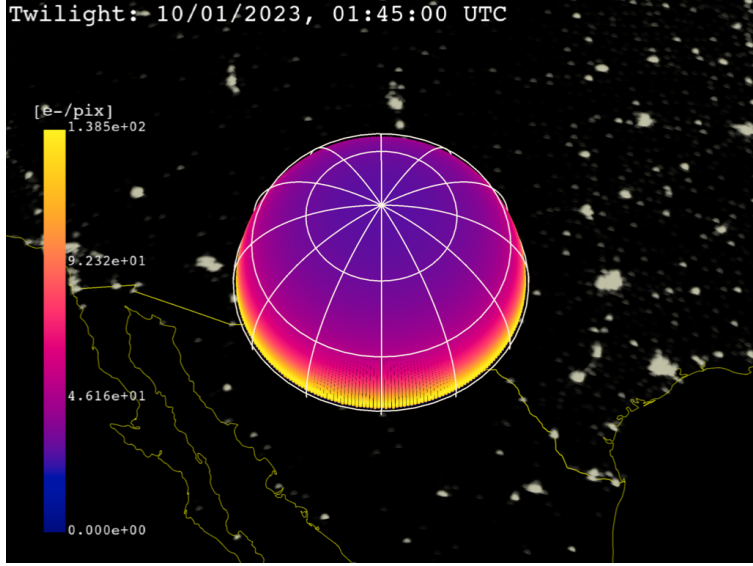


Figure 6.6. Mean twilight signal on the local observer hemisphere. The observer is in New Mexico, USA at 32.900° N, -105.533° W

6.1.6 Scattered Moonlight

Moonlight scattering through the atmosphere significant increases background brightness [42]. This scattering effect can be decomposed into Rayleigh (isotropically distributed) and Mie (exponentially distributed) scattering modes. The Rayleigh scattered component is computed with Table 4 published by Daniels parameterized by the angle from the observation to zenith z_{obs} , the angle from the Moon to zenith z_{moon} , and the angle between the observation and the Moon on the horizon ΔAz [51]. Interpolating this table yields the intensity of the Rayleigh scattering F_{rs} in $10^{-10} \text{ W}/(\text{cm}^2 \cdot \mu\text{m} \cdot \text{sr})$ [42]. The Mie scattered component is formulated with Eq 6.9.

$$F_{ms}(\lambda) = a_1 \left[e^{-\left(\frac{\Psi}{\Psi_1}\right)} + a_2 e^{-\left(\frac{\pi-\Psi}{\Psi_2}\right)} \right] F_{rs}(\lambda) \quad (6.9)$$

Daniels recommends $a_1 \in [50, 100]$, $a_2 \in [0.01, 0.02]$, $\Psi_1 \in [10^{\circ}, 20^{\circ}]$, and $\Psi_2 \approx 50$ [51]. Prior to any station-specific fitting, the middle of these intervals are chosen, yielding $a_1 = 75$, $a_2 = 0.015$, $\Psi_1 = 15^{\circ}$, and $\Psi_2 = 50^{\circ}$. a_1 and a_2 are dimensionless, such that F_{ms} also has

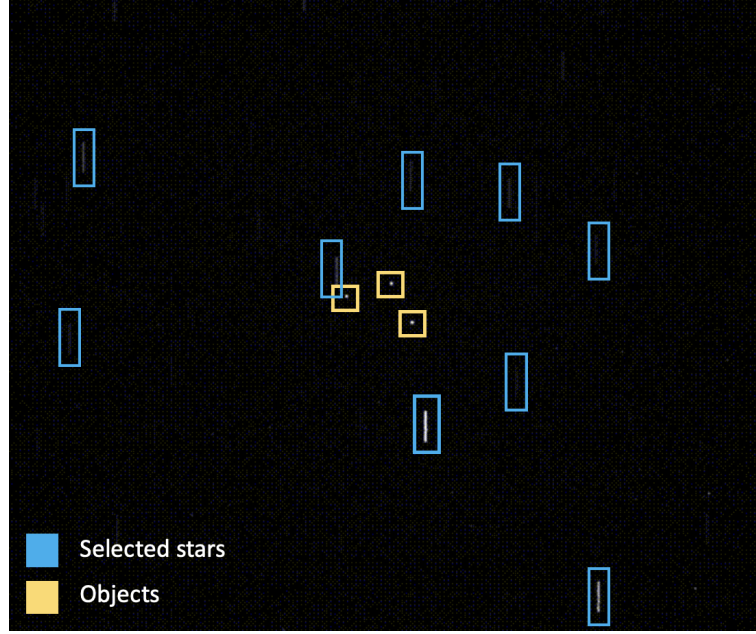


Figure 6.7. Raw image of three GEO objects with stars streaking through the background. As expected the star signals have a variety of signal-to-noise ratios. Taken by the Purdue Optical Ground station at $32.900^\circ \text{ N}, -105.533^\circ \text{ W}$ by Nathan Houtz.

units of $10^{-10} \text{ W}/(\text{cm}^2 \cdot \mu\text{m} \cdot \text{sr})$. The total intensity of the scattered moonlight F_{mt} via Eq 6.10 following Krag's formulation [42].

$$F_{mt} = f(\theta) [F_{rs}(\lambda) + F_{ms}(\lambda)] \quad (6.10)$$

in Eq 6.10, $f(\theta)$ is the lunar phase function which describes the fraction of the full Moon brightness reflected at an observer when the Sun-Moon-observer angle is θ . This function is linearly interpolated within Table 3 in [51]. Finally, Krag introduces a correction factor f_{corr} to account for the difference between the Sun's irradiance spectrum and the spectrum of scattered moonlight, defined in Eq 6.11.

$$f_{corr} = \frac{I_0}{SUN(550 \text{ [nm]})} \quad (6.11)$$

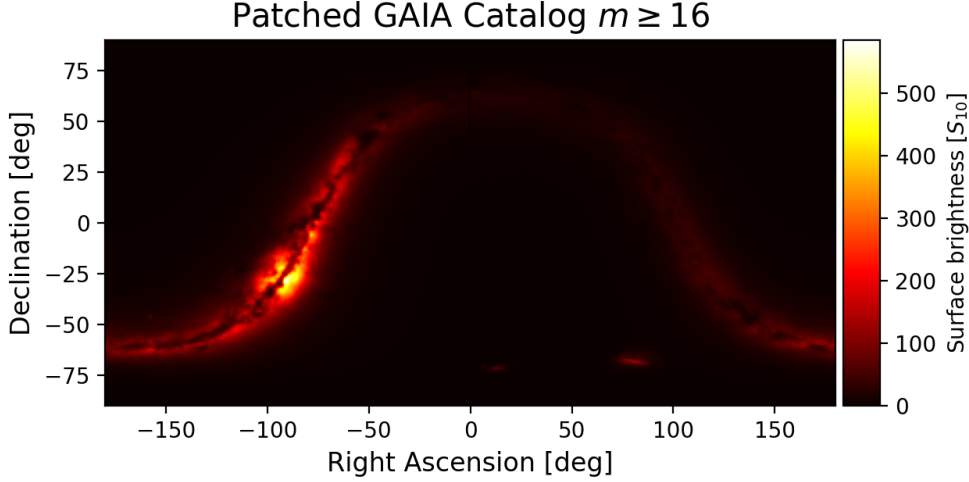


Figure 6.8. Integrated starlight brightness map

With all these pieces, the mean scattered moonlight signal in ADU per pixel is computed in Eq 6.12.

$$\bar{S}_{moon} = F_{mt}(550 \text{ [nm]}) \cdot SINT \cdot \left(\frac{s_{pix}}{3600} \right)^2 \cdot \Delta t \cdot f_{corr} \quad (6.12)$$

6.1.7 Zodiacal Light

Zodiacal light is an effect created by sunlight reflecting off of dust in the ecliptic plane [42]. Zodiacal light is strongest around the Sun — an exclusion zone for most optical telescopes — but also reaches a peak directly away from the Sun due to the opposition effect. This peak is known as the Gegenschein, meaning "opposing light". The zodiacal light brightness is linearly interpolated within Table 1 of [52] which is listed for convenience in Appendix

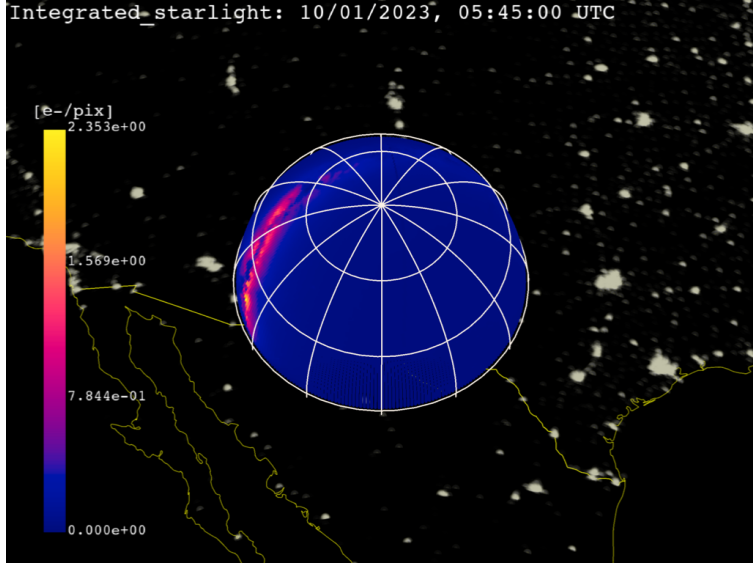


Figure 6.9. Integrated starlight signal on the local observer hemisphere. The observer is in New Mexico, USA at 32.900° N, -105.533° W

11.1.1. This reports the surface brightness of the zodiacal light in S_{10} , which is used without conversion to find the mean CCD signal in ADU per pixel via Eq 6.13.

$$\bar{S}_{zod} = BINT \cdot \left(\frac{s_{pix}}{3600} \right)^2 \cdot \Delta t \cdot ZOD \cdot 10^{-4} \quad (6.13)$$

As in the integrated starlight signal, the 10^{-4} factor reconciles the S_{10} surface brightness with the 0th magnitude source in BINT.

6.1.8 Background Sampling

The background signals are only defined in terms of their means, as each signal models the expected amount of radiation without accounting for the quantized nature of light [42]. Since light is transmitted in individual photons, their incidence on a given pixel will follow a statistical distribution. Assuming that each photon does not interact with others, the incidence of a photon on a pixel is well-modeled as a Poisson process for each background term [3]. This distribution models the number of independent and identically distributed events that occur during a time period. For CCD astronomy, this translates to the event of

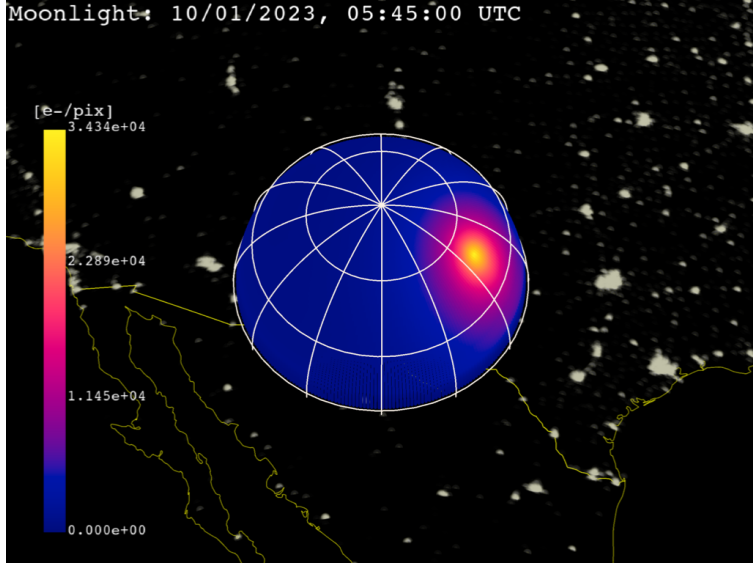


Figure 6.10. Mean scattered moonlight signal on the local observer hemisphere. The observer is in New Mexico, USA at 32.900° N, -105.533° W

a photon hitting the sensor. A Poisson distribution is defined on the positive integers by a single parameter λ which is both the mean and variance of the distribution. The probability density function (PDF) for the Poisson distribution takes the form of Eq 6.14 [3].

$$P_{\lambda}(x = k) = \frac{\lambda^k e^{-\lambda}}{k!} \quad (6.14)$$

This distribution has a useful property that $P_{\lambda_1+\lambda_2}(x = k) = P_{\lambda_1}(x = k) + P_{\lambda_2}(x = k)$ so long as the distributions described by λ_1 and λ_2 are independent. Our background sources are reasonably assumed to be independent as they each originate from distinct physical processes.

$$\lambda_{background} = \bar{S}_{airglow} + \bar{S}_{pollution} + \bar{S}_{twilight} + \bar{S}_{star} + \bar{S}_{moon} + \bar{S}_{zod} \quad (6.15)$$

Drawing samples from the Poisson distribution defined by $\lambda_{background}$ computes the background of the CCD image.

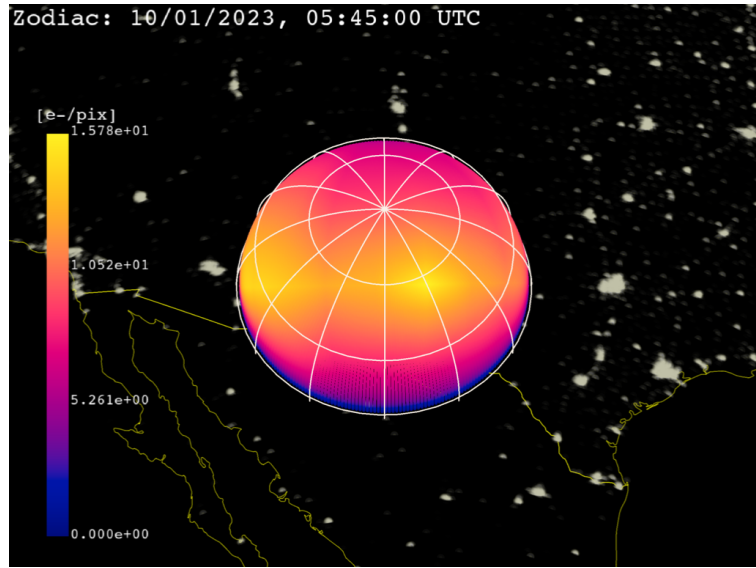


Figure 6.11. Mean zodiacal light signal on the local observer hemisphere. The observer is in New Mexico, USA at 32.900° N, -105.533° W

6.2 Sensor Effects

6.2.1 Dark Noise

TODO

6.2.2 Readout Noise

TODO

6.3 Signal to Noise Ratio (SNR)

TODO

6.4 Sampling Noisy Light Curves

TODO

7. Light Curve Simulation

7.1 Dynamics

7.1.1 Orbital Dynamics

SGP4

TODO

7.2 Implicit and Explicit Shape Representations

A computer can represent 3D objects implicitly or explicitly. An implicit representation might be the solution to an algebraic equation, i.e., $x^2 + y^2 + z^2 = 1$ defines a sphere of radius 1 centered at the origin. Often, a shape may be defined by a set of signed distance functions (SDFs). An SDF takes in a point in \mathbb{R}^3 and outputs the distance from the object, returning negative distance if the queried point is inside the shape. The object can then be rendered via ray marching. A ray is cast from the camera out into the scene for each pixel of the screen, each performing distance queries along its length until it intersects the object or diverges.

By contrast, an explicit shape representation creates complex 3D geometry from simple 2D building blocks. In the most common case, object faces are defined by triangles. This means that at the scale of the individual faces, the shape is always composed of flat surfaces that meet at sharp angles. While this can add complexity to many fields of shape analysis and geometry processing, triangulated surfaces are perfect for our application. Human-made space objects like most satellites are composed of flat faces, with the exception of parabolic antennas and cylindrical rocket bodies.

7.3 The Wavefront OBJ File Format

One common text file format for 3D model files is `.obj`, developed by Wavefront Technologies in the early 1990s [53]. Each OBJ file consists of a list of vertex positions and face definitions, with optional vertex normals and tangents. An `.obj` listing for a cube is included for reference in Appendix 11.1.3. Given the vertex positions and adjacency infor-

mation stored in the model file, useful properties of the object can be computed for use later in both light curve simulation and shape inversion. For each triangular face F_i of the model defined by vertices $F_i = \{v_1, v_2, v_3\}$, the outward-pointing face normal is computed with

$$\hat{n} = \frac{(v_2 - v_1) \times (v_3 - v_1)}{\|(v_2 - v_1) \times (v_3 - v_1)\|_2}. \quad (7.1)$$

The face area is computed with

$$a = \frac{\|(v_2 - v_1) \times (v_3 - v_1)\|_2}{2}. \quad (7.2)$$

The support of each face — the perpendicular distance from the origin to the plane defining the face — is computed with

$$h = v_1 \cdot \hat{n}. \quad (7.3)$$

The volume of the entire object is compute with

$$\frac{1}{3} \sum_{i=0}^{|F|} \vec{h}_i \cdot \vec{a}_i. \quad (7.4)$$

In Eq 7.4, $|F|$ is the number of faces defining the object. \vec{h} and \vec{a} are column vectors collecting all face supports and areas. The Extended Gaussian Image, a quantity defined in 8.1.1, is computed row-wise for the i th face with

$$\vec{E}_i = \vec{a}_i \vec{n}_i. \quad (7.5)$$

7.4 Selected Satellite Models

Most of the analysis in this work used one of the 3D model files shown in Figure 7.1. Figure 7.1 highlights the size of the GEO communications satellites (TELSTAR, HYLAS, Hispasat, and ASTRA). In contrast, the LEO satellites (Starlink and Landsat) are dwarfed at the left end of the lineup.

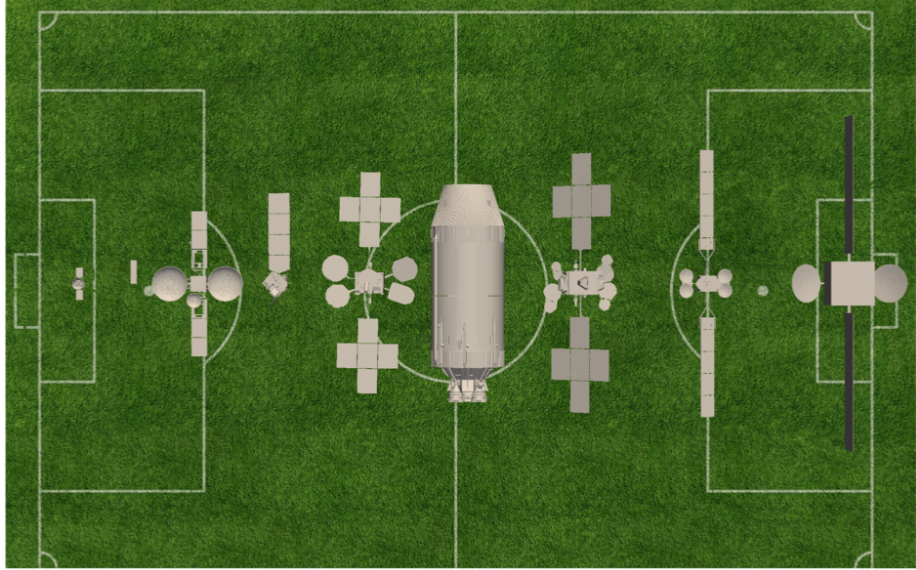


Figure 7.1. Selected space objects with soccer field for size reference. In order, the objects are TESS, Starlink V1, TDRS, Landsat 8, Hispasat 30W-6, Saturn V SII, TELSTAR 19V, HYLAS 4, and simplified ASTRA.

7.5 The Bidirectional Reflectance Distribution Function

Although light curves come from unresolved measurements, the interactions that produce them are directly driven by the shape and material properties of the object being observed. In order to simulate accurate light curves, all relevant optical interactions must be modeled. In broad terms, this boils down to determining how the object is illuminated, how it casts shadows on itself, and how it is observed.

At the microscopic scale, the surface of an object is composed of facets — small areas sharing a normal vector. The macroscopic optical properties of the material is driven by the distribution of sizes and normal directions of these microfacets. If the facet normals are distributed in biased orientations, the macroscopic surface may show anisotropy, leading to the appearance of brushed metal. If the facets normals are at large angles to each other, the

surface may appear dull as the direction of the outgoing light may be largely independent from the incoming direction. Subsurface effects — where incoming light rays scatter *inside* the surface can also change the macroscopic properties of the material.

This discussion raises an important question; how should the macroscopic outcomes of the microscopic interactions of incident light on a surface be modeled? The bidirectional reflectance distribution function (BRDF) is a tool from computer graphics that addresses this problem. The BRDF is a function on the hemisphere which expresses the fraction of light per solid angle (radiance \mathcal{R}) leaving the surface in a given direction, divided by the incident power per unit area (irradiance \mathcal{I}). The general formulation for a BRDF f_r is given by Eq 7.6 [54].

$$f_r(\mathbf{x}, L \rightarrow O) = \frac{d\mathcal{R}(\mathbf{x} \rightarrow O)}{d\mathcal{I}(L \rightarrow \mathbf{x})} \quad (7.6)$$

In Eq 7.6, $\mathbf{x} \in \mathbb{R}^3$ is the point on the object's surface where the BRDF is evaluated. $L \in \mathbb{S}^2$ is the incoming illumination unit vector and $O \in \mathbb{S}^2$ is the outgoing unit vector. Note that this work treats $f_r(\mathbf{x}, L \rightarrow O)$ and $f_r(L \rightarrow O)$ as equivalent in later descriptions, leaving the evaluation point \mathbf{x} implied. This definition is useful for building intuition about the form of the BRDF, but to represent a physically plausible reflection process, a candidate function must satisfy three additional constraints. A physically plausible BRDF must conserve energy — more energy cannot be reflected from the surface than was incident on it. It must also be reciprocal — switching the observer and illumination directions should not change the BRDF value as the surface interaction. This reciprocity is sometimes known as the *Helmholtz Reciprocity Rule* in literature [55]. Finally, plausible BRDFs are positive — they take on nonnegative values for all valid inputs [55]. A surface cannot reflect negative light, so this should feel natural. Explicitly, energy conservation is expressed by Eq 7.7 [55].

$$\forall L \in \mathbb{S}^2 : \int_{O \in \mathbb{S}^2} f_r(L \rightarrow O) d\mathbb{S}^2 \leq 1 \quad (7.7)$$

Eq 7.7 states that for all possible illumination directions L , integrating all possible outgoing observer directions O on the unit sphere cannot return greater than one from the energy conservation integral. Reciprocity can also be formalized via 7.8.

$$\forall L, O \in \mathbb{S}^2 : f_r(L \rightarrow O) = f_r(O \rightarrow L) \quad (7.8)$$

7.5.1 BRDF Formulations

Now that the requirements for a plausible physical BRDF have been established, a collection of commonly-used BRDFs can be presented. The following BRDFs are all energy conserving, reciprocal, and nonnegative. *Caveat emptor*: this does not mean that they are always sufficient for modeling real-world materials, they merely represent ways hypothetical surfaces could reflect light without breaking any fundamental physics.

Lambertian

The simplest BRDF is one that reflects equally in all directions. This BRDF is termed Lambertian or diffuse.

$$f_r(L \rightarrow O) = \frac{C_d}{\pi} \quad (7.9)$$

In Eq 7.9, $0 \leq C_d \leq 1$ is the surface's coefficient of diffuse reflection. For example, $C_d = 0.4$ means that the surface reflects 40% of incident radiation and absorbs the other 60%.

Phong

While the diffuse BRDF reflects energy isotropically, many real-world reflections are highly biased. At the extreme end, a perfect mirror reflection is effectively a Dirac delta function in the reflected illumination direction. Many real-world materials are well-modeled as a linear combination of diffuse and specular effects. A simple specular BRDF model is that developed by Phong in 1975 [56]. The Phong model splits the BRDF into a Lambertian term governed by C_d and a specular term governed by the coefficient of specular reflection $0 \leq C_s \leq 1$ and the specular exponent $n \geq 0$ [54].

$$f_r(L \rightarrow O) = \frac{C_d}{\pi} + \frac{C_s \frac{n+2}{2\pi} (O \cdot R)^n}{N \cdot L} \quad (7.10)$$

In Eq 7.10, R is the reflected illumination vector, computed via $R = 2(N \cdot L)N - L$. As n increases, the specular glint becomes sharper and more intense, eventually approaching a perfectly mirror reflection. Because of the introduction of a new coefficient of reflection, a new constraint is needed to maintain energy conservation. Because C_d and C_s each represent the *fraction* of light reflected in each mode, it should be clear that $C_d + C_s \leq 1$. This can also be reformulated with an explicit coefficient of absorption C_a which captures the fraction of incident radiation absorbed by the surface, yielding $C_d + C_s + C_a = 1$.

Blinn-Phong

The Blinn-Phong BRDF is similar to the Phong BRDF, but parameterizes the specular lobe in terms of the halfway vector H [54]. This vector is halfway between the illumination and observer directions such that $H = L + O$ which needs to be normalized before use. As the halfway vector approaches the surface normal vector, the observer must be approaching the reflected illumination vector, leading to a more intense specular highlight.

$$f_r(L \rightarrow O) = \frac{C_d}{\pi} + \frac{C_s \frac{n+2}{2\pi} (N \cdot H)^n}{4(N \cdot L)(N \cdot O)} \quad (7.11)$$

Glossy

TODO

Cook-Torrance

TODO

Oren-Nayar

TODO

Ashikhmin-Shirley

TODO

Summary

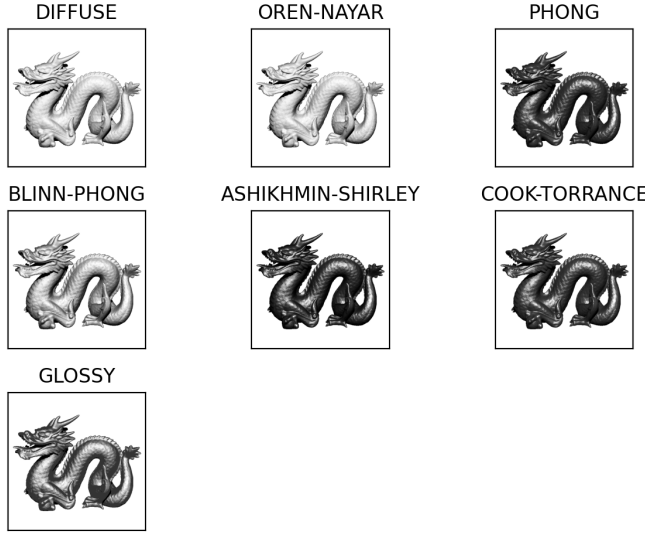


Figure 7.2. Implemented BRDFs rendered with arbitrary parameters, demonstrating the qualitative differences between lighting models

7.6 Simulating Convex Objects

Light curve simulation for convex geometry can be solved semi-analytically as each face's contribution to the measured irradiance can be computed individually [8]. Determining whether a face is illuminated requires two horizon checks to determine visibility from the Sun and to the observer. For a face i at timestep j these horizon checks are expressed by the shadowing condition μ_{ij} .

$$\mu_{ij} = \begin{cases} 1 & \text{if } (O_j \cdot \hat{n}_i) > 0 \text{ and } (L_j \cdot \hat{n}_i) > 0 \text{ and } \delta_{ij,ss} = 0 \text{ and } \delta_{ij,os} = 0 \\ 0 & \text{otherwise} \end{cases} \quad (7.12)$$

The unit vectors O and L point from the center of mass of the object to the observer and Sun, respectively. We choose the outward-pointing face normal unit vector \hat{n} by convention for all mesh operations. The self-shadowing and observer-shadowing conditions, $\delta_{ij,ss}$ and $\delta_{ij,os}$, are always zero for convex polyhedra but are crucial for accurately simulating non-convex geometry. For objects with concavities, self-shadowing refers to shadows cast by an object onto itself and observer-shadowing refers to otherwise visible faces blocked by other portions of the geometry.

The irradiance I received by the observer at timestep j is the sum of the received irradiance from all faces, composed of specular and diffuse contributions. Each contribution is expressed as the product of the normalized irradiance \hat{I} . This can be scaled to adjust for the distance from the observer to the object to yield the noiseless received irradiance.

TODO: add L = Ga stuff

7.7 Simulating Non-Convex Objects

Many existing light curve simulation methods for non-convex objects rely on ray tracing schemes like Möller and Trumbore’s ray-triangle intersection algorithm [4], [57]. This computation has complexity $\mathcal{O}(n^2)$ if implemented naïvely, but can be improved to $\mathcal{O}(n \ln n)$ with better spatial data structures. For human-made space objects, there may be significant self-shadowing at large phase angles. As a result, it cannot be assumed that the self-shadowing conditions $\delta_{ij,ss}$ and $\delta_{ij,os}$ are zero [4], [14]. Naïve ray traced shadows generally require $\mathcal{O}(n^2)$ ray-triangle intersections per timestep for n faces. For this reason, ray traced shadows quickly become infeasible for complex objects without GPU parallelization. The limitations of ray-triangle intersections for light curve simulation is discussed at length by Frueh et al. [14].

7.7.1 The Importance of Self-Shadowing

To motivate the need for accurate shadows when dealing with human-made space objects, consider the error introduced by neglecting shadows for different types of space objects. Kaasalainen and Torppa’s work on asteroids reasonably assumed that shadowing was a

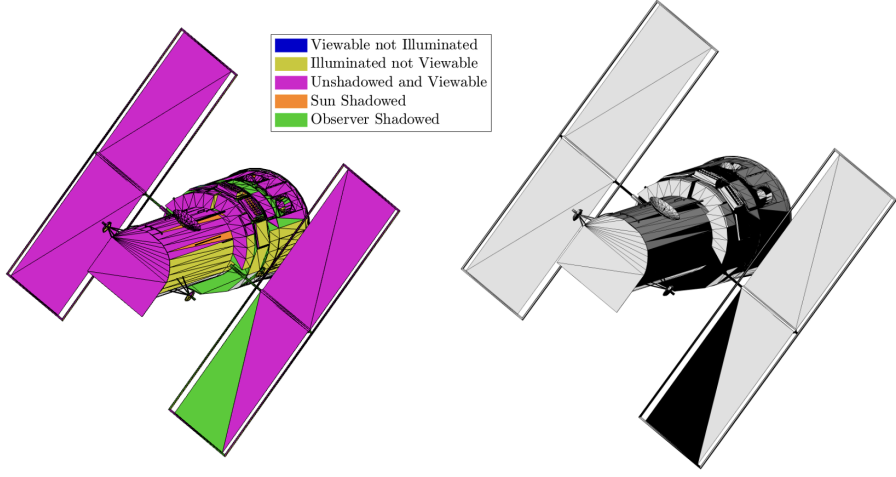


Figure 7.3. Hubble Space Telescope ray traced shadow categorization and shading. Models from [58]

negligible contribution to the measured light curve. Human-made objects do not afford the same luxury. Figure 7.4 displays light curves for the asteroid Bennu and the Hubble Space Telescope with and without accurate shadows under a single-axis spin profile with inertially fixed Sun and observer vectors. Without accurate shadowing, the light curve's intensity and its time derivative can be significantly error-prone.

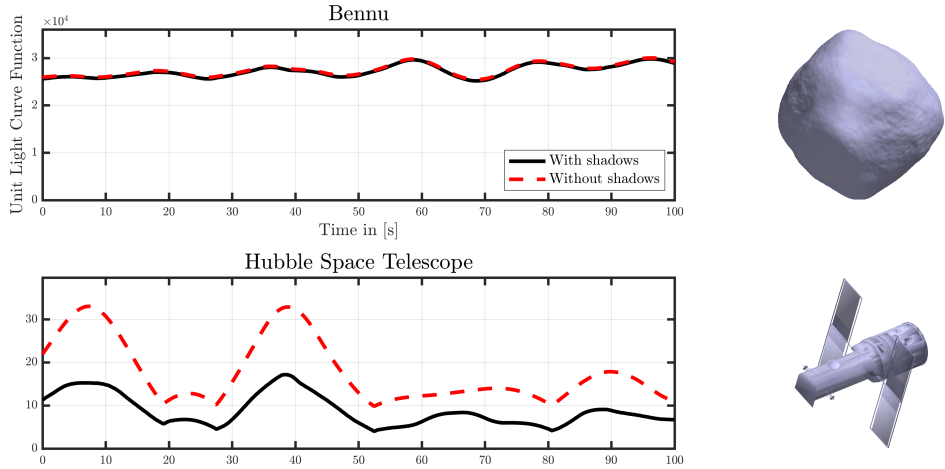


Figure 7.4. Brightness errors introduced by neglecting shadows for Bennu and HST. Models from [58]

7.7.2 Shadow Mapping

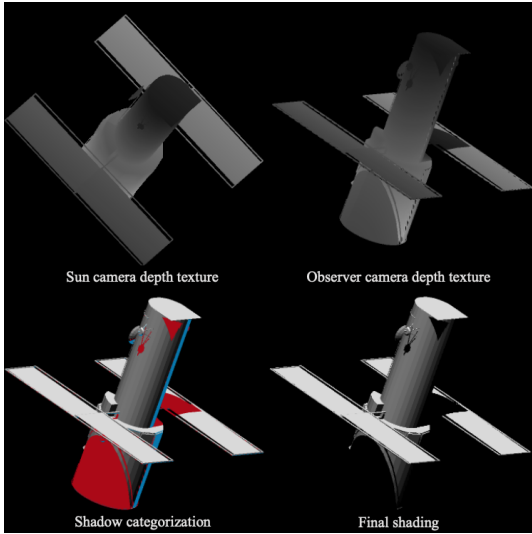


Figure 7.5. Hubble Space Telescope shadow mapping with self (red) and horizon (blue) shadows rendered. Models from [58]

TODO: remake 7.5 with figure from Python.

In the LightCurveEngine, shadow mapping is used for faster and more accurate self-shadowing. Shadow mapping is a well understood technique in computer graphics [59]. Although modern ray traced shadowing may be more computationally efficient, shadow mapping was selected for its ease of implementation [59]. Because shadow mapping shades individual pixel fragments instead of entire faces, it offers increasing shadow quality over facewise ray tracing as the number of mesh faces falls.

Given an observer and Sun vector in the body frame of the object, shadow mapping proceeds in a four step process. In step one, a camera is positioned along the Sun vector and a perpendicular depth texture is computed. In the second step, depth values in Sun camera space are transformed to observer camera space, where a second depth texture is computed. This second texture is used to find the closest fragment along each ray to the Sun [60]. Self-shadowed fragments are classified as those further from the Sun than the closest fragment along the same ray, indicated in red in Figure 7.5. Fragments that do not pass the convex shadowing condition are horizon shadowed, indicated in blue in Figure 7.5,

determining the Sun and observer shadowing conditions at once. All remaining fragments are shaded with using the same Lambertian reflection model in ?? TODO: this equation is broken. Computing the light curve function for the final rendered image requires summing all pixel values and dimensionalizing the result by the area of the observer camera's field of view. The light curve simulation environment used in this work was implemented in C and OpenGL using raylib [61].

TODO: add algorithm pseudocode for lighting shader

8. Light Curve Shape Inversion

8.1 Direct Convex Shape Inversion

Traditionally, direct light curve inversion involves two distinct optimization problems: a linear least squares problem to fit an EGI to the measured light curve, and a second optimization to produce accurate vertex positions and face adjacency information [4]. The first problem is data-driven and linear, using the observations to estimate a plausible EGI. The second problem is highly nonlinear but convex and requires significant tuning for robust convergence [26].

8.1.1 The Extended Gaussian Image

The discrete EGI $\vec{E} \in \mathbb{R}^{m \times 3}$ is composed of m unit vectors \hat{n} each scaled a nonnegative scalar $a \in \mathbb{R}$, $a_i \geq 0$ [62].

$$\vec{E}_i = a_i \hat{n}_i \quad (8.1)$$

In the context of shape inversion, the m vectors \hat{n} should be a relatively uniform tessellation of the unit sphere. A convex polytope can be uniquely represented by an EGI of facet normal vectors scaled by each facet's area. The set of normal vectors in an EGI is denoted \mathcal{N} with the set of areas denoted \mathcal{A} . The vector of facet areas is denoted $\vec{a} \in \mathbb{R}^{m \times 1}$. The norm of the EGI is notated $\|\vec{E}\| = \vec{a}$ with the ‘size’ of the EGI $\|\vec{E}\| = m$.

The solution to the Minkowski problem proves the existence and uniqueness of a convex polytope for any EGI satisfying the closure condition in Eq 8.2 [63]. Equivalently, an EGI uniquely represents a closed, convex polyhedron — a polytope — with no open boundaries, up to a translation.

$$\sum_{i=1}^m a_i \hat{n}_i = [0, 0, 0] \quad (8.2)$$

While a given EGI uniquely represents a polytope, that same EGI could also be interpreted to be an infinite number of non-convex and open geometries. An example of this extended family is depicted in Figure 8.1.

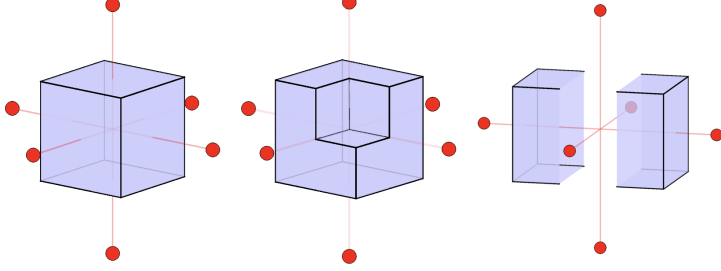


Figure 8.1. Simplified convex, non-convex, and open EGI nonuniqueness. Larger circles indicate greater relative areas assigned to a given normal vector.

8.1.2 EGI Optimization

The EGI fulfills two important criteria for the shape inversion problem: it can be estimated directly from the light curve, attitude profile, and material properties, and uniquely represents a convex object [8]. Further, the EGI can be transformed into a unique convex object and vice versa through the dual transform and Minkowski problem [63], [64].

Given a light curve, direct shape inversion schemes sample m candidate normal vectors \hat{n} on the unit sphere to fit an EGI to the observed light curve $\vec{L}_{\text{ref}} \in \mathbb{R}^{n \times 1}$ [4], [12]. This is accomplished by solving an optimization problem to distribute the area vector \vec{a} across the sampled normals to minimize the residual between the observed and modeled light curves. In practice, this is a constrained nonnegative least squares problem and can be solved efficiently for large numbers of normal vectors and light curve data points:

TODO: add description of NNLS and FNNLS

$$\min_{\vec{a}} \|\vec{L}_{\text{ref}} - G\vec{a}\|_2 \quad \text{subject to } \vec{a}_i \geq 0. \quad (8.3)$$

It is important to note that the area estimated with Eq 8.3 is necessarily *albedo-area* due to the diffuse reflectivity coefficient C_d in Eq. ???. If the value of C_d is uniform but unknown, the recovered geometry will incorrectly scaled without impacting the face adjacency or relative feature sizes.

The convex reflection matrix $G \in \mathbb{R}^{n \times m}$ with ijth entries G_{ij} defined at time i for each facet j is defined as the normalized received facet irradiance per unit facet area:

$$[g]_{ij} = \frac{I_{ij}}{I_0 a_j}. \quad (8.4)$$

This relationship between the object irradiance and area defines the normalized convex light curve \vec{L}_{convex} , that produced by a convex object of facet areas \vec{a} under the attitude profile and lighting conditions that yield G .

$$\vec{L}_{\text{convex}} = G \vec{a} \quad (8.5)$$

The optimization in Eq. 8.3 produces a coarse approximation of the true EGI as m is finite. Increasing m necessarily improves the quality and sparsity of the estimated EGI, but at the cost of computational resources. The estimation was performed using a synthetic light curve input from $n = 500$ Sun and observer vectors uniformly sampled on the sphere in the body frame, producing a full rank G matrix. $m = 500$ candidate normal vectors were sampled using a spherical Fibonacci mapping described by Keinert et al. in [65]. Results are visualized for an icosahedron in the body frame in Figure 8.2. Reconstructing the object at this stage is difficult due to the quantity of faces present in the estimated EGI.

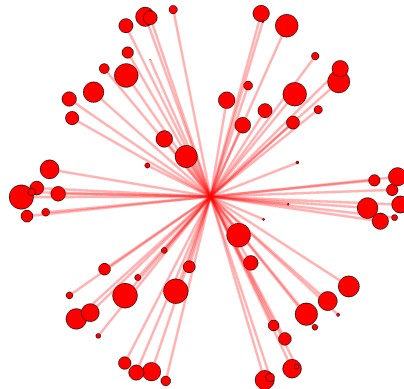


Figure 8.2. Initial icosahedron EGI optimization before resampling

TODO: re-do this figure with 2-sphere in python 8.2

8.1.3 EGI Resampling

We propose a normal vector resampling step to promote a more accurate and sparse EGI. The normal vectors used in Eq. 8.2 are generally correct, with each group clustering around a normal vector of the truth geometry. This clustering behavior occurs when none of the candidate normal vectors are sufficiently close to the truth. Resampling in a cone centered on each initial EGI normal vector provides more accurate candidates for EGI estimation. This process mimics a single optimization step with a much larger m , where the coarse EGI is used to exclude areas on the sphere with little or no normal area.

Uniformly sampling a cone of half-angle ϕ is accomplished by strategically sampling points on the unit sphere.

$$\hat{n}_{cone} = \begin{bmatrix} \sqrt{1-z^2} \cos \theta \\ \sqrt{1-z^2} \sin \theta \\ z \end{bmatrix} \quad (8.6)$$

In Eq. 8.6 two coordinates are chosen $z \in [\cos \phi, 1]$ and $\theta \in [0, 2\pi)$, yielding a point uniformly distributed on a cone of half-angle ϕ about the central axis $[0, 0, 1]^T$ [66]. These points are then rotated using a direction cosine matrix to center the cone on an axis of interest. The axis of rotation for this transformation is the cross product of the original central axis $[0, 0, 1]^T$ with the final axis \hat{n}_{cone} with the rotation angle θ being the angle between the same two vectors. This means that we can define the principal rotation parameter form of this transformation, which can be converted into the DCM using Eq 3.7 and 3.5, as

$$\begin{aligned} \theta &= \cos^{-1}(\hat{n}_{cone,z}) \\ \lambda &= \hat{n}_{cone} \times [0, 0, 1]^T. \end{aligned} \quad (8.7)$$

The number of new candidates sampled per initial solution vector and the cone half-angle should be adjusted on a case-by-case basis depending on the compute power available and light curve data quality. Multiple iterative methods exist for solving nonnegatively

constrained least squares (NNLS) problems. The classical NNLS algorithm was published by Lawson and Hanson and improved later by Bro and De Jong in their Fast NNLS (FNNLS) approach [67], [68].

Existing EGI optimization schemes like those of Fan [4], Friedman [12], and Cabrera [18] are limited by a single normal vector sampling step, leading to a lack of sparsity in the optimized EGI. High-density normal vector sampling in regions known to contain non-zero area leads to EGI solutions that are generally more sparse and cluster more tightly about true normal vectors.

This process is shown in Figure 8.3 for the same icosahedron with a half-angle $\phi = \frac{\pi}{20}$ and sampling density of 50 candidate vectors per cone.

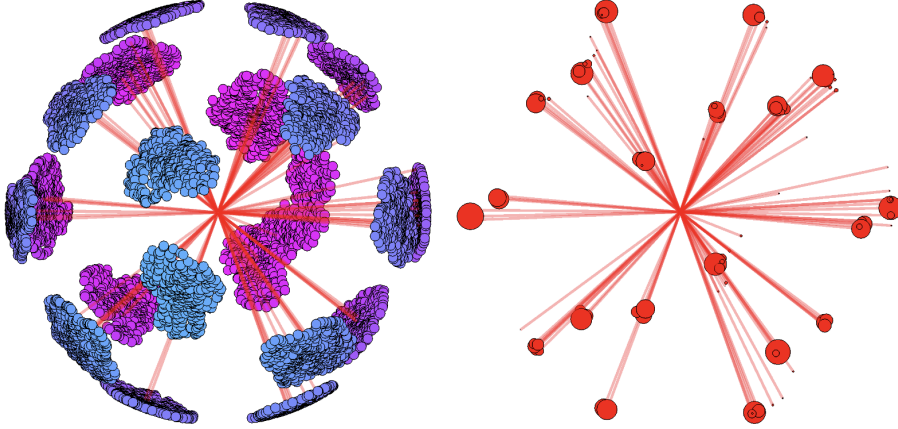


Figure 8.3. Resampled normal vectors (left) with reoptimized EGI (right)

TODO: remake this figure with 2-sphere

8.1.4 EGI Merging

After resampling and reoptimizing with Eq. 8.3, the reestimated EGI is merged by computing all groups \mathcal{G} of EGI vectors within an angular offset α :

$$\mathcal{G}_k = \left\{ \vec{E}_i \in \vec{E} \mid \cos^{-1} \left(\frac{\hat{E}_i \cdot \hat{E}_k}{\|\vec{E}_i\| \|\vec{E}_k\|} \right) < \alpha \right\}. \quad (8.8)$$

In practice, the choice of α is dependent on the user's tolerance for discretization, as merging will approximate smooth geometry by discrete faces with normal vectors offset by 2α . Groups are merged by summing all group members, yielding a single EGI vector \vec{E}_m without loss of closure.

$$\vec{E}_m = \sum_{\vec{E} \in \mathcal{G}_k} \vec{E} \quad (8.9)$$

Merging the resampled EGI using Figure ?? with $\alpha = \frac{\pi}{10}$ produces a final sparse EGI fit for object reconstruction, shown in Figure 8.4.

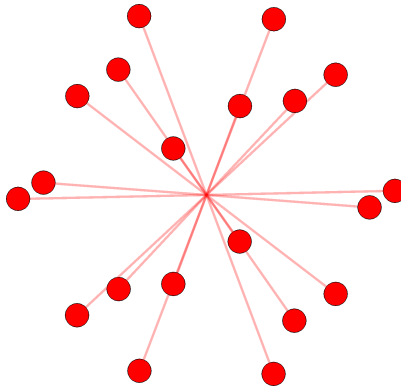


Figure 8.4. Merged icosahedron EGI

TODO: remake with true EGI on the right

8.1.5 Geometry Recovery from the EGI

At this stage, the resampled and merged EGI encodes a convex approximation of the underlying object with no guarantee of the closure of this EGI. The EGI closure constraint Eq. ?? motivates a simple procedure to correct an invalid EGI by adding the mean closure error to each entry:

$$\vec{E}_{\text{closed}} = \vec{E}_{\text{open}} - \sum_{i=1}^m a_i \hat{n}_i. \quad (8.10)$$

The concept of a closure step is not a novel contribution. Fan's method solved an problem to adjust the EGI towards closure [4]. This process is improved with a simpler analytical

correction. In practice, this process should be performed before each reconstruction to accelerate convergence. Failing to correct non-closed EGIs will cause convergence to a nonzero minimum in the reconstruction objective function as there is no corresponding convex object with the given EGI.

The unique convex object encoded by each closed EGI is reconstructed by solving for the polytope's set of vertices \mathcal{V} and faces \mathcal{F} encoding the adjacency relations between vertices. This is accomplished following the procedure introduced by Little through the dual transformation [62]. The dual set \mathcal{D} are vertices in $(A, B, C) \in \mathbb{R}^3$ that satisfy the following plane condition for a point (x, y, z) on each face of the object:

$$Ax + By + Cz + 1 = 0 \quad (8.11)$$

If (x, y, z) are chosen to be the closest points in the object's planes to the origin, the dual set \mathcal{D} can be expressed in terms of the EGI and a support vector $\vec{h} \in \mathbb{R}^{\|\mathcal{F}\| \times 1}$, as expressed in Eq 8.12. The support vector is the perpendicular distance of each face defining the object to the origin.

$$\mathcal{D} = \frac{\vec{E}}{\|\vec{E}\| \vec{h}} \quad (8.12)$$

The object's vertices \vec{v}_{ref} are found by solving a linear system of equations for each face on the convex hull of dual set vertices. Triplets of vertices on the resulting faces are used to find a single real vertex by intersecting the three planes defining the dual set vertices.

$$\begin{bmatrix} v_{ref,x} \\ v_{ref,y} \\ v_{ref,z} \end{bmatrix} = \begin{bmatrix} v_{i,x} & v_{j,x} & v_{k,x} \\ v_{i,y} & v_{j,y} & v_{k,y} \\ v_{i,z} & v_{j,z} & v_{k,z} \end{bmatrix}^{-1} \begin{bmatrix} 1 \\ 1 \\ 1 \end{bmatrix} \quad (8.13)$$

Convex face adjacency information is found by triangulating the convex hull of all reference vertices. The accuracy of the recovered geometry is entirely dependent on the correctness of the support vector \vec{h} used to produce the dual set. Finding the true support vector is the challenge of the final optimization in convex shape inversion.

8.1.6 Support Vector Optimization

Prior work by Fan used Little's objective function for support vector optimization [4], [62].

$$f(\vec{h})_{\text{Little}} = \vec{h} \cdot \vec{a} \quad (8.14)$$

TODO: description of the optimization

8.2 Non-Convex Feature Inversion

8.2.1 Non-Convex Feature Detection and Location

Many human-made space objects are, as highlighted in Figure ??, highly non-convex. As a result, their shape inversion is plagued by the fact that the Minkowski problem-driven reconstruction methods of Eq ?? cannot recover non-convex features. Instead of beginning from the ground up, the convex shape guess can be leveraged to detect and locate concavities.

We can retain information about large, unilateral object concavities during EGI estimation in Eq. 8.3 by relaxing the EGI closure constraint. This unconstrained form is also generally functional for most convex objects and can be used without loss of detail in the final reconstruction as long as closure correction in Eq. 8.9 is still employed.

The mean axis of prominent concave features is determined by measuring the divergence of the optimized EGI from a closed object with the magnitude of the closure error \vec{e}_{EGI} .

$$\vec{e}_{EGI} = - \sum_{i=1}^m a_i \hat{n}_i. \quad (8.15)$$

The EGI closure error vector in Eq 8.15 represents the missing area on each body axis that could be added to close the object. The addition of the minus sign transforms the vector from expressing the presence of excess area to the absence of missing area. The closure error will be negligible if there are no concavities present. The closure error may also be negligible if there is no self-shadowing is present over the sampled attitude profile, therefore the closure error merely quantifies the self-shadowing that is occurring, not whether there may be self-shadowing in other orientations.

Under the strong assumption that the concavities present are major and unilateral, this EGI error vector points along the mean axis of the concavity.

TODO: replace this analytic relationship (which is bad and wrong) with an iteration to minimize LC error

8.2.2 Concavity Creation

Our process for creating an accurate concavity in the reconstructed convex guess proceeds in four major steps. The model is first subdivided to add more faces and vertices. Subdivided vertices are then classified by their proximity to the EGI error vector, indicating whether their positions should be updated. Boundary vertices are identified, and vertex positions are updated based on the estimated internal angle computed via Eq. ??.

Model Subdivision

Subdividing the initial convex object guess is essential for retaining object detail during concavity creation. A combination of linear subdivision, Loop subdivision, and remeshing algorithms are used to accomplish this. Linear subdivision is advantageous when object faces are equally sized and boundary edges must be maintained. Loop subdivision is preferable when there are numerous vertices so that subdivisions do not drastically diverge from the initial boundary surface. Loop subdivision softens sharp edges as it relies on B-splines to interpolate new vertex positions [69]. The specific type and resolution of subdivision used depends on the level of detail the user needs to maintain in the introduced concavity, although linear subdivision followed by Loop subdivision is a useful baseline. Varying combinations of subdivision are shown in Figure 8.5 to illustrate the available configurations.

Vertex Classification and Displacement

When introducing a concavity, it is important to classify which vertices are part of the concave feature — and therefore need to be updated — and which vertices should remain unaffected. This is accomplished by measuring the angle from each face normal to the EGI error vector, where faces with normal vectors within an angle of $\pi/2$ to the error vector

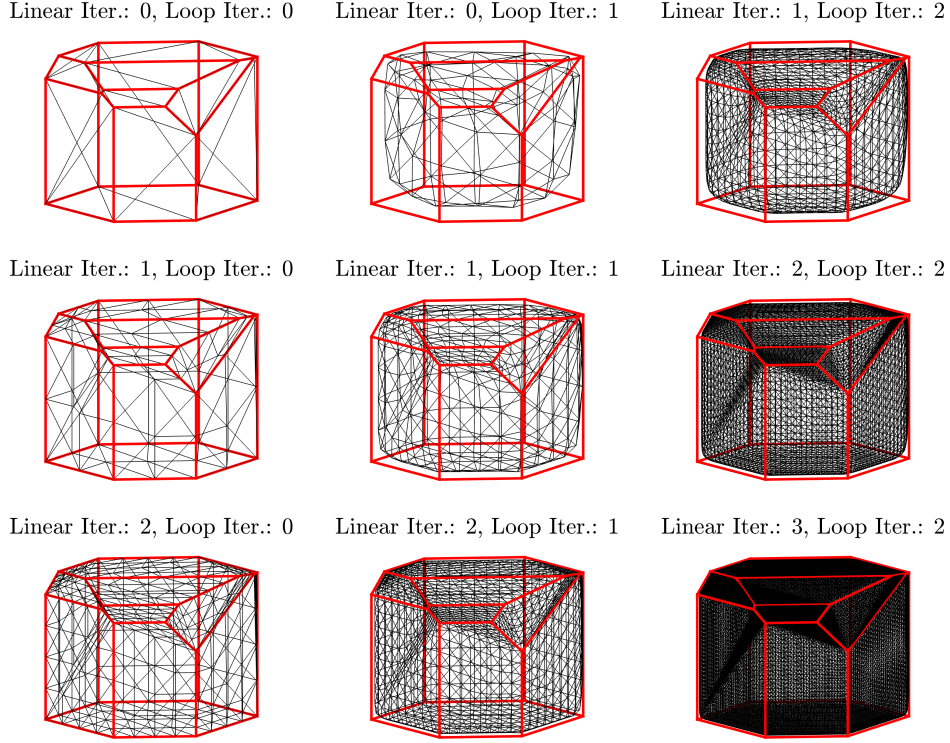


Figure 8.5. Subdivided object (black) with reference (red) with various levels of subdivision

must be updated. In reality, all face normals and areas are impacted by the presence of the concavity in the area optimization Eq. 8.3 and EGI correction step Eq. 8.10. Selecting the angle deflect $\pi/2$ updates all faces above the horizon from the EGI error vector. This bound tends to produce visually accurate concavities. Faces requiring an update are termed *free* faces, with all others termed *root* faces.

Vertices on free faces are further classified as being *root-adjacent* or *free*. Root-adjacent vertices are part of at least one root face, whereas free vertices belong to only free faces. Classifying vertices in this way results in a border of root-adjacent vertices around the interior free vertices, visualized in Figure 8.6.

Given the estimated internal angle ψ_{est} and the error vector $\hat{\mathbf{e}}_{EGI}$, each i th free vertex is displaced to introduce a geometrically accurate concavity by moving each a distance d_i in the direction of $-\hat{\mathbf{e}}_{EGI}$:

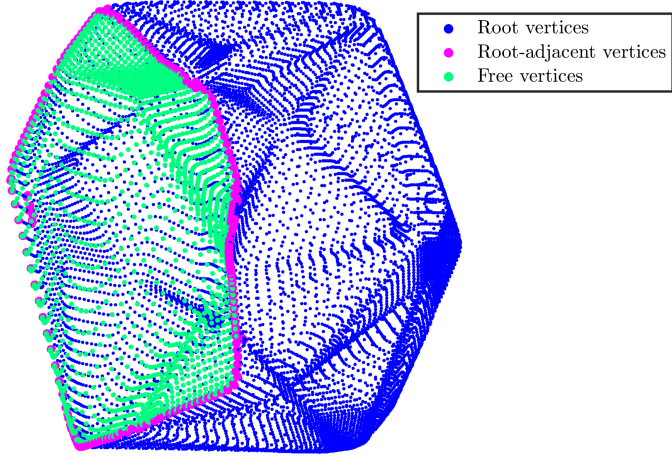


Figure 8.6. Root-adjacent and free vertices

$$d_i = p_i \sqrt{\csc^2 \frac{\psi_{est}}{2} - 1}, \quad (8.16)$$

where p_i is the distance from each i th free vertex to the nearest root-adjacent vertex.

8.3 Object Reconstruction Results

Displacing free vertices in the EGI error vector direction by d_i yields accurate concavities for objects whose concave boundaries lie in a plane. The result of applying this process to a set of representative convex objects is shown in Figure 8.7 using the same attitude profiles and as in Figure ??.

The collapsed cube and icosahedron in Figure 8.7 are recovered effectively, but the collapsed house and box-wing satellite expose two limitations of the vertex displacement technique. In the case of the house where the concavity boundary is not constrained to a plane, the edges of the created concave feature are incorrect. The box-wing satellite's shadowing geometry leads the convex guess to be a poor approximation of the geometry outside of the concavity while also inheriting the same problem as the house.

This vertex displacement scheme will negligibly impact the convex guess if the truth object is also convex. A convex truth object will produce a small $\|\vec{e}_{EGI}\|$, causing the vertex

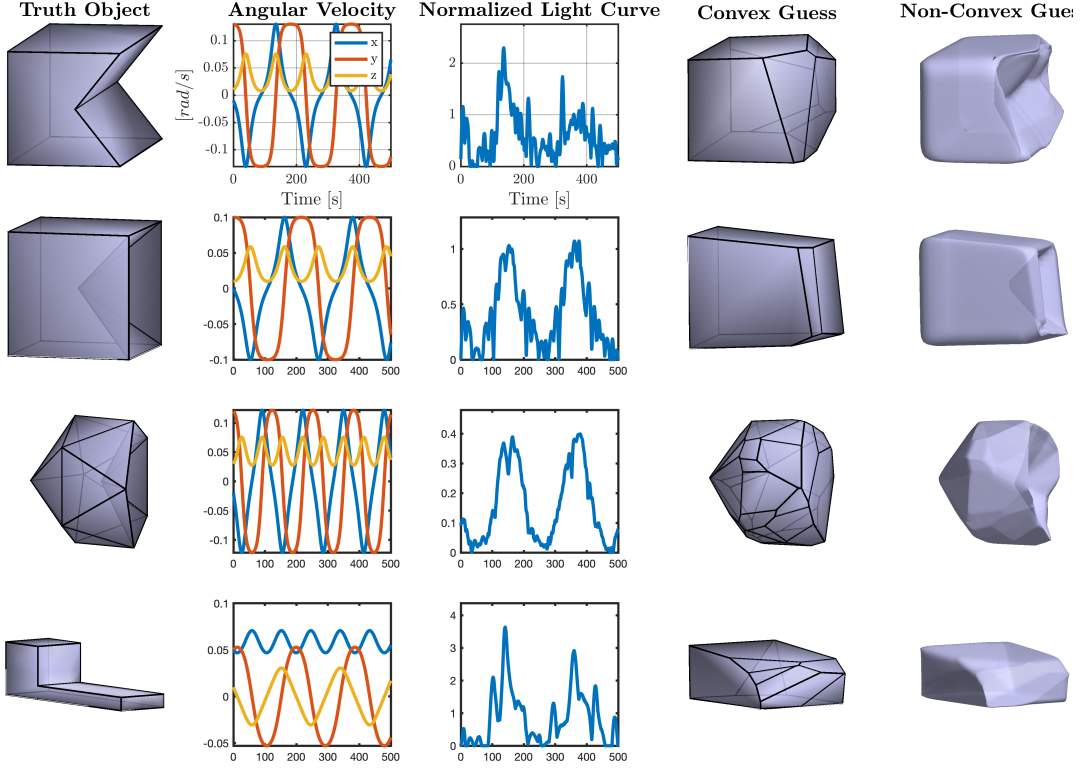


Figure 8.7. Collapsed house, cube, icosahedron, and box-wing satellite reconstructions using vertex displacement

update depth d_i to trend towards zero as the estimated internal angle approaches $\psi = 180^\circ$. This is illustrated in Figure 8.8 using the same input convex objects and attitude profiles as in Figure ??.

Figure 8.8 clearly displays the compatibility of vertex displacement with truly convex objects. All objects are reconstructed faithfully in both their convex and non-convex inversions, with the same caveats noted in the discussion following Figure ???. Some truly sharp edges are rounded during mesh subdivision as seen in the gem or rectangular prism. That said, others like the cylinder become more accurate as subdivision reintroduces continuity lost to discretization in EGI merging.

8.4 Shape Inversion With Noisy Measurements

TODO: write

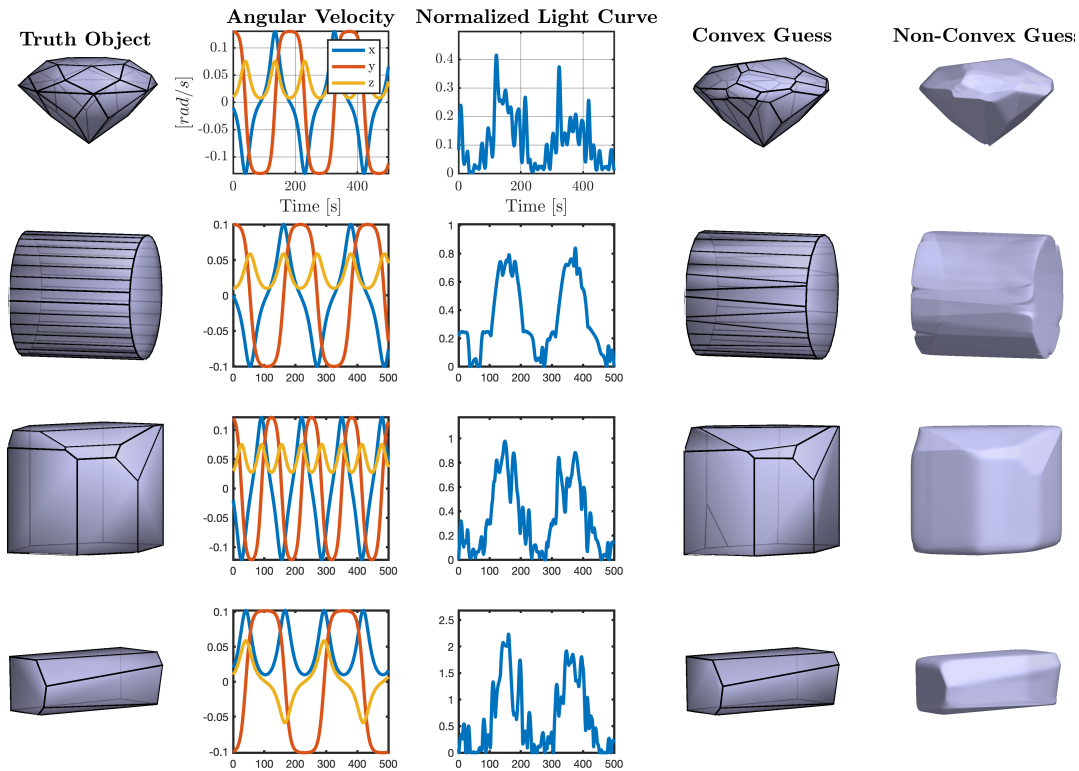


Figure 8.8. Convex objects under vertex displacement procedure

9. Recommendations

10. Future Work

11. Appendices

11.1 Astronomical Spectra Data

Atmospheric Extinction

```
{"lambda": [0.0, 3.2e-07, 3.400000000000003e-07, 3.6e-07, 3.799999999999996e-07,  
4e-07, 4.5e-07, 5e-07, 5.5e-07, 6e-07, 6.5e-07, 7e-07, 8e-07, 0.001], "extinction":  
[5.0, 0.96, 0.54, 0.42, 0.34, 0.27, 0.17, 0.13, 0.11, 0.11, 0.07, 0.05, 0.03, 0.0]}{}
```

Quantum Efficiency

```
# Wavelength [m], quantum efficiency [non-dim]
```

```
350.70422535211264e-9, 0.23880597014925387
```

```
361.9718309859155e-9, 0.27761194029850755
```

```
369.01408450704224e-9, 0.34925373134328375
```

```
378.8732394366197e-9, 0.37910447761194044
```

```
390.14084507042253e-9, 0.39104477611940314
```

```
398.59154929577466e-9, 0.41492537313432853
```

```
409.85915492957747e-9, 0.4477611940298508
```

```
419.71830985915494e-9, 0.43880597014925393
```

```
430.9859154929577e-9, 0.43880597014925393
```

```
439.4366197183098e-9, 0.4507462686567165
```

```
449.2957746478873e-9, 0.43880597014925393
```

```
459.15492957746477e-9, 0.43880597014925393
```

```
480.28169014084506e-9, 0.5134328358208956
```

```
488.7323943661972e-9, 0.5402985074626867
```

```
500e-9, 0.5492537313432837
```

```
509.85915492957747e-9, 0.5761194029850747
```

```
521.1267605633802e-9, 0.5940298507462688
```

```
539.4366197183099e-9, 0.5940298507462688
```

```
550.7042253521126e-9, 0.6000000000000001
```

```
561.9718309859154e-9, 0.5940298507462688
```

```
590.1408450704225e-9, 0.5910447761194031
```

```
601.4084507042253e-9, 0.555223880597015
```

```
611.2676056338028e-9, 0.5582089552238807
```

```
629.5774647887324e-9, 0.5164179104477613
```

```
640.8450704225352e-9, 0.5164179104477613
```

```
650.7042253521126e-9, 0.4746268656716419
```

```
669.0140845070423e-9, 0.43880597014925393
```

```
680.2816901408451e-9, 0.4358208955223881
```

```
690.1408450704225e-9, 0.40298507462686584
```

```
700e-9, 0.42089552238805983
```

```
708.450704225352e-9, 0.4119402985074627
```

```
721.1267605633802e-9, 0.4238805970149254
```

```
729.5774647887324e-9, 0.37910447761194044
```

```
739.4366197183099e-9, 0.3880597014925373
```

```
749.2957746478874e-9, 0.35820895522388063
```

```
760.5633802816901e-9, 0.34626865671641793
```

```
770.4225352112676e-9, 0.36119402985074645
```

11.1.1 Background Source Data

Lunar Phase Factor

```
{"phase_factor": [1.00, 0.809, 0.685, 0.483, 0.377, 0.288, 0.225, 0.172, 0.127, 0.089, 0.061, 0.041, 0.077, 0.017, 0.009, 0.004, 0.001, 0.0, 0.0], "phase_angle": [0, 0.17453293, 0.34906585, 0.52359878, 0.6981317, 0.87266463, 1.04719755, 1.22173048, 1.3962634, 1.57079633, 1.74532925, 1.91986218, 2.0943951, 2.26892803, 2.44346095, 2.61799388, 2.7925268, 2.96705973, 3.14159265]}
```

Scattered Moonlight

```
{"z_obs": [0.0, 0.17453292519943295, 0.3490658503988659, 0.5235987755982988, 0.6981317007977318, 0.8726646259971648, 1.0471975511965976, 1.2217304763960306, 1.3962634015954636], "delta_az": [0.0, 0.7853981633974483, 1.5707963267948966, 2.356194490192345, 3.141592653589793], "z_moon": [0.0, 0.5235987755982988, 1.0471975511965976, 1.3089969389957472], "radiance": [[[22.0, 19.0, 13.0, 10.0], [22.0, 19.0, 13.0, 10.0], [22.0, 19.0, 13.0, 10.0], [22.0, 19.0, 13.0, 10.0]], [[22.0, 21.0, 15.0, 11.0], [22.0, 20.0, 14.0, 11.0], [22.0, 19.0, 13.0, 10.0], [22.0, 18.0, 12.0, 9.7], [22.0, 18.0, 12.0, 9.6]], [[22.0, 23.0, 18.0, 13.0], [22.0, 22.0, 16.0, 12.0], [22.0, 19.0, 14.0, 10.0], [22.0, 17.0, 12.0, 9.9], [22.0, 17.0, 12.0, 10.0]], [[22.0, 25.0, 21.0, 16.0], [22.0, 23.0, 18.0, 14.0], [22.0, 20.0, 14.0, 11.0], [22.0, 17.0, 12.0, 11.0], [22.0, 28.0, 25.0, 20.0], [23.0, 25.0, 21.0, 17.0], [23.0, 21.0, 16.0, 12.0], [23.0, 17.0, 14.0, 13.0], [23.0, 16.0, 14.0, 14.0]], [[24.0, 31.0, 31.0, 25.0], [24.0, 28.0, 26.0, 20.0], [24.0, 22.0, 18.0, 15.0], [24.0, 18.0, 17.0, 16.0], [24.0, 18.0, 18.0, 18.0]], [[27.0, 37.0, 39.0, 33.0], [27.0, 33.0, 32.0, 26.0], [27.0, 25.0, 22.0, 18.0], [27.0, 22.0, 22.0, 21.0], [27.0, 22.0, 25.0, 26.0]], [[34.0, 47.0, 54.0, 48.0], [34.0, 41.0, 43.0, 37.0], [34.0, 33.0, 29.0, 25.0], [34.0, 30.0, 33.0, 32.0], [34.0, 31.0, 40.0, 40.0]], [[55.0, 72.0, 89.0, 82.0], [55.0, 65.0, 71.0, 63.0], [55.0, 54.0, 50.0, 43.0], [55.0, 54.0, 61.0, 58.0], [58.0, 58.0, 76.0, 75.0]]]}
```

Zodiacal Light

```
{"ecliptic_lat": [0.0, 0.17453292519943295, 0.3490658503988659, 0.5235987755982988, 0.6981317007977318, 0.8726646259971648, 1.0471975511965976, 1.2217304763960306, 1.3962634015954636], "ecliptic_lon": [3.141592653589793, 2.792526803190927, 2.443460952792061, 2.0943951023931953, 1.7453292519943295, 1.3962634015954636, 1.1344640137963142, 1.0471975511965976, 0.9599310885968813, 0.8726646259971648, 0.7853981633974483, 0.6981317007977318, 0.6108652381980153, 0.5235987755982988, 0.4363323129985824, 0.3490658503988659, 0.2617993877991494, 0.17453292519943295, 0.08726646259971647, 0.0], "brightness": [[[258.0, 211.0, 206.99999999999997, 239.0, 277.0, 365.0, 535.0, 630.0, 756.0, 939.0, 1190.0, 1490.0, 2010.0000000000002, 2940.0, 4660.0, 7690.000000000001, 15100.0, 36500.0, 176000.0, 163000000.0], [212.0, 194.0, 185.0, 217.0, 247.0000000000003, 312.0, 418.0, 455.0, 512.0, 603.0, 696.0, 825.0, 1150.0, 1550.0, 1820.0, 2140.0, 2760.0, 2720.0, 5630.0, 19900.0], [183.0, 174.0, 168.0, 196.0, 220.0000000000003, 258.0, 330.0, 339.0, 358.0, 403.0, 442.0, 512.0, 635.0, 800.0, 932.0, 1070.0, 1120.0, 1390.0, 1700.0, 2290.0], [159.0, 153.0, 152.0, 177.0, 196.0, 219.0, 258.0, 270.0, 282.0, 290.0, 304.0, 331.0, 363.0, 417.0, 491.0, 542.0, 592.0, 655.0, 724.0, 794.0], [141.0, 137.0, 137.0, 161.0, 175.0, 190.0, 204.0, 212.0, 229.0, 227.0, 233.0, 240.0, 224.0000000000003, 241.0, 246.0, 252.0, 265.0, 290.0, 315.0, 403.0], [127.0, 127.0, 128.0, 146.0, 156.0, 166.0, 165.0, 166.0, 183.0, 185.0, 189.0, 186.0, 171.0, 180.0, 183.0, 186.0, 190.0, 199.0, 209.0, 252.0], [117.0, 120.0, 120.0, 132.0, 139.0, 146.0, 137.0, 137.0, 147.0, 149.0, 150.0, 149.0, 137.0, 141.0, 144.0, 145.0, 145.0, 145.0, 146.0, 150.0], [110.0000000000001, 112.0000000000001, 112.0000000000001, 120.0, 123.0, 127.0, 118.0, 120.0, 124.0, 124.0, 124.0, 126.0, 118.0, 120.0, 121.0, 121.0, 121.0, 121.0, 121.0], [103.0, 105.0, 105.0, 108.0, 111.0000000000001, 111.0000000000001, 106.0, 107.0, 107.0, 108.0, 107.0, 111.0000000000001, 107.0, 106.0, 108.0, 108.0, 108.0, 108.0, 108.0]]}
```

Parameter	Value
FWHM	1.5
Sensor dimensions	$0.03690 \times 0.03690 [m]$
<i>f</i> number	7.2
Aperture diameter	$0.35560 [m]$
Secondary diameter	$0.1724660 [m]$
Sensor pixels	4096×4096
Pixel size	$9.009 \cdot 10^{-6} [m/\text{pix}]$
Pixel scale	$0.72545 [\text{arcsec}]$
Field of view	$0.824425^\circ \times 0.824425^\circ$
Integration time	1 [s]

Table 11.1. Purdue Optical Ground Station telescope parameters

11.1.2 Telescope Parameters

Purdue Optical Ground Station

11.1.3 File Formats

Wavefront OBJ Example

```
# Blender v2.92.0 OBJ File: ''
# www.blender.org
mtllib cube.mtl
o Cube_Cube.003
v 1.000000 1.000000 -1.000000
v 1.000000 1.000000 1.000000
v 1.000000 -1.000000 -1.000000
v 1.000000 -1.000000 1.000000
v -1.000000 1.000000 -1.000000
v -1.000000 1.000000 1.000000
v -1.000000 -1.000000 -1.000000
v -1.000000 -1.000000 1.000000
vt 0.625000 0.000000
vt 0.375000 0.250000
vt 0.375000 0.000000
vt 0.625000 0.250000
vt 0.375000 0.500000
vt 0.625000 0.500000
vt 0.375000 0.750000
vt 0.625000 0.750000
vt 0.375000 1.000000
vt 0.125000 0.750000
vt 0.125000 0.500000
vt 0.875000 0.500000
vt 0.625000 1.000000
vt 0.875000 0.750000
vn 1.0000 0.0000 0.0000
vn 0.0000 -1.0000 0.0000
vn -1.0000 0.0000 0.0000
vn 0.0000 1.0000 0.0000
vn 0.0000 0.0000 -1.0000
vn 0.0000 0.0000 1.0000
usemtl None
s off
f 2/1/1 3/2/1 1/3/1
f 4/4/2 7/5/2 3/2/2
f 8/6/3 5/7/3 7/5/3
f 6/8/4 1/9/4 5/7/4
f 7/5/5 1/10/5 3/11/5
f 4/12/6 6/8/6 8/6/6
f 2/1/1 4/4/1 3/2/1
f 4/4/2 8/6/2 7/5/2
f 8/6/3 6/8/3 5/7/3
f 6/8/4 2/13/4 1/9/4
f 7/5/5 5/7/5 1/10/5
f 4/12/6 2/14/6 6/8/6
```

REFERENCES

- [1] N. G. S. F. Center, *Vanguard 1*, <https://nssdc.gsfc.nasa.gov/nmc/spacecraft/display.action?id=1958-002B>, Accessed: 2023-09-04.
- [2] D. Vallado, *Fundamentals of Astrodynamics and Applications*, 4th ed. J. Wertz, Ed. Microcosm Press, Mar. 2013.
- [3] C. Frueh, *Space traffic management*, Lecture Notes, 2019.
- [4] S. Fan, “The light curve simulation and its inversion problem for human-made space objects,” Ph.D. dissertation, Purdue University, Aug. 2020. DOI: [10.25394/PGS.12749570.v1](https://doi.org/10.25394/PGS.12749570.v1).
- [5] A. Burton and S. Fan, “Mapping the solution space for light curve attitude estimation,” *43rd COSPAR Scientific Assembly. Held 28 January-4 February*, vol. 43, p. 2193, 2021.
- [6] H. N. Russell, “On the light-variations of asteroids and satellites,” *The Astrophysical Journal*, vol. 24, no. 1, pp. 1–18, 1906.
- [7] M. Kaasalainen and J. Torppa, “Optimization methods for asteroid lightcurve inversion: I. shape determination,” *Icarus*, vol. 153, no. 1, pp. 24–36, 2001, ISSN: 0019-1035. DOI: <https://doi.org/10.1006/icar.2001.6673>. [Online]. Available: <https://www.sciencedirect.com/science/article/pii/S0019103501966734>.
- [8] M. Kaasalainen, J. Torppa, and K. Muinonen, “Optimization methods for asteroid lightcurve inversion: II. the complete inverse problem,” *Icarus*, vol. 153, no. 1, pp. 37–51, 2001, ISSN: 0019-1035. DOI: <https://doi.org/10.1006/icar.2001.6674>. [Online]. Available: <https://www.sciencedirect.com/science/article/pii/S0019103501966746>.
- [9] J. urech and M. Kaasalainen, “Photometric signatures of highly nonconvex and binary asteroids,” *Astronomy & Astrophysics*, vol. 404, no. 2, pp. 709–714, Jun. 2003. DOI: [10.1051/0004-6361:20030505](https://doi.org/10.1051/0004-6361:20030505).
- [10] M. Kaasalainen, J. urech, and V. Sidorin, *DAMIT: Database of Asteroid Models from Inversion Techniques*, Astrophysics Source Code Library, record ascl:1412.004, Dec. 2014. ascl: [1412.004](https://ascl.net/1412.004).

- [11] S. Fan, C. Frueh, and A. Buzzoni, “A light curve simulation of the apollo lunar ascent module,” in *AIAA/AAS Astrodynamics Specialist Conference*, 2016, pp. 1–10. doi: [10.2514/6.2016-5504](https://doi.org/10.2514/6.2016-5504).
- [12] A. M. Friedman, “Observability analysis for space situational awareness,” Ph.D. dissertation, Purdue University, Apr. 2020. doi: [10.25394/PGS.12196863.v1](https://doi.org/10.25394/PGS.12196863.v1).
- [13] D. Kobayashi and C. Frueh, “Compressed sensing for satellite characterization,” in *Proceedings of the 20th AAS/AIAA Astrodynamics Specialist Conference*, Aug. 2020, pp. 1–20.
- [14] C. Früh and M. K. Jah, “Coupled orbit attitude motion of high area-to-mass ratio (hamr) objects including efficient self-shadowing,” *Acta Astronautica*, vol. 95, pp. 227–241, 2014, ISSN: 0094-5765. doi: <https://doi.org/10.1016/j.actaastro.2013.11.017>.
- [15] J. Allworth, L. Windrim, J. Wardman, D. Kucharski, J. Bennett, and M. Bryson, “Development of a high fidelity simulator for generalised photometric based space object classification using machine learning,” in *Proceedings of 70th International Astronautical Congress*, International Astronautical Congress, 2019, pp. 1–14. doi: [10.48550/ARXIV.2004.12270](https://arxiv.org/abs/2004.12270). [Online]. Available: <https://arxiv.org/abs/2004.12270>.
- [16] J. Allworth, L. Windrim, J. Bennett, and M. Bryson, “A transfer learning approach to space debris classification using observational light curve data,” *Acta Astronautica*, vol. 181, pp. 301–315, Jan. 2021. doi: [10.1016/j.actaastro.2021.01.048](https://doi.org/10.1016/j.actaastro.2021.01.048).
- [17] R. Furfaro, R. Linares, and V. Reddy, “Shape Identification of Space Objects via Light Curve Inversion Using Deep Learning Models,” in *Proceedings of the 20th Advanced Maui Optical and Space Surveillance Technologies Conference*, S. Ryan, Ed., Sep. 2019, 17, p. 17.
- [18] D. V. Cabrera, J. Utzmann, and R. Förstner, “Inversion of the shape of space debris from non-resolved optical measurements within spook,” in *Proceedings of the 22nd Advanced Maui Optical and Space Surveillance Technologies Conference*, 2021, pp. 1–18.
- [19] B. K. Bradley and P. Axelrad, “Lightcurve inversion for shape estimation of geo objects from space-based sensors,” in *Proceedings of the International Symposium on Space Flight Dynamics*, 2014, pp. 1–20.

- [20] R. Linares and J. L. Crassidis, “Space-object shape inversion via adaptive hamiltonian markov chain monte carlo,” *Journal of Guidance, Control, and Dynamics*, vol. 41, no. 1, pp. 47–58, 2018.
- [21] K. McNally, D. Ramirez, A. M. Anton, D. Smith, and J. Dick, “Artificial intelligence for space resident objects characterisation with lightcurves,” in *Proceedings of the 8th European Conference on Space Debris*, ESA Space Debris Office, 2021, pp. 1–12.
- [22] L. D. J. Blacketer, “Attitude characterisation of space objects using optical light curves,” Ph.D. dissertation, University of Southampton, Mar. 2022. [Online]. Available: <https://eprints.soton.ac.uk/457200/>.
- [23] M. Kaasalainen and J. Torppa, “Optimization methods for asteroid lightcurve inversion: I. shape determination,” *Icarus*, vol. 153, no. 1, pp. 24–36, 2001, ISSN: 0019-1035. DOI: <https://doi.org/10.1006/icar.2001.6673>. [Online]. Available: <https://www.sciencedirect.com/science/article/pii/S0019103501966734>.
- [24] C.-K. Chng, M. Sasdelli, and T.-J. Chin, “Globally optimal shape and spin pole determination with light-curve inversion,” *Monthly Notices of the Royal Astronomical Society*, vol. 513, no. 1, pp. 311–332, Jan. 2022, ISSN: 0035-8711. DOI: [10.1093/mnras/stac198](https://doi.org/10.1093/mnras/stac198). eprint: <https://academic.oup.com/mnras/article-pdf/513/1/311/43446894/stac198.pdf>. [Online]. Available: <https://doi.org/10.1093/mnras/stac198>.
- [25] B. Calef, J. Africano, B. Birge, D. Hall, and P. Kervin, “Photometric signature inversion,” in *Unconventional Imaging II*, V. L. Gamiz, P. S. Idell, and M. S. Strojnik, Eds., International Society for Optics and Photonics, vol. 6307, SPIE, 2006, pp. 141–150. DOI: [10.1117/12.683015](https://doi.org/10.1117/12.683015). [Online]. Available: <https://doi.org/10.1117/12.683015>.
- [26] S. Fan and C. Frueh, “A direct light curve inversion scheme in the presence of measurement noise,” *The Journal of the Astronautical Sciences*, vol. 67, Aug. 2019. DOI: [10.1007/s40295-019-00190-3](https://doi.org/10.1007/s40295-019-00190-3).
- [27] S. Fan and C. Frueh, “Multi-hypothesis light curve inversion scheme for convex objects with minimal observations,” in *Proceedings of the 8th European Conference on Space Debris*, ESA Space Debris Office, 2021, pp. 1–7.
- [28] A. M. Friedman and C. Frueh, “Observability of light curve inversion for shape and feature determination exemplified by a case analysis,” *Journal of the Astronautical Sciences*, vol. 69, no. 2, pp. 537–569, Apr. 2022. DOI: [10.1007/s40295-021-00293-w](https://doi.org/10.1007/s40295-021-00293-w).

- [29] R. Linares, M. Jah, and J. Crassidis, “Inactive space object shape estimation via astrometric and photometric data fusion,” *Advances in the Astronautical Sciences*, vol. 143, pp. 217–232, Jan. 2012.
- [30] R. Linares, M. K. Jah, J. L. Crassidis, and C. K. Nebeleky, “Space object shape characterization and tracking using light curve and angles data,” *Journal of Guidance, Control, and Dynamics*, vol. 37, no. 1, pp. 13–25, 2014. DOI: [10.2514/1.62986](https://doi.org/10.2514/1.62986).
- [31] R. Linares and R. Furfaro, “Space object classification using deep convolutional neural networks,” in *19th International Conference on Information Fusion*, Jul. 2016, pp. 1–8.
- [32] E. Kerr, G. P. Elisabeth, P. Talon, and D. Petit, “Using ai to analyse light curves for geo object characterisation,” in *Proceedings of the 22nd Advanced Maui Optical and Space Surveillance Technologies Conference*, 2021, pp. 1–9.
- [33] D. Hall, B. Calef, K. Knox, M. Bolden, and P. Kervin, “Separating attitude and shape effects for non-resolved objects,” in *The 2007 AMOS Technical Conference Proceedings*, Maui Economic Development Board, Inc. Kihei, Maui, HI, 2007, pp. 464–475.
- [34] D. O. Fulcoly, K. I. Kalamaroff, and F. K. Chun, “Determining basic satellite shape from photometric light curves,” *Journal of Spacecraft and Rockets*, vol. 49, pp. 76–82, 2012.
- [35] T. Yanagisawa and H. Kurosaki, “Shape and motion estimate of leo debris using light curves,” *Advances in Space Research*, vol. 50, no. 1, pp. 136–145, 2012, ISSN: 0273-1177. DOI: <https://doi.org/10.1016/j.asr.2012.03.021>.
- [36] D. Kobayashi and C. Frueh, “Compressed sensing for satellite characterization: Shadowing as a sensing matrix,” *8th European Conference on Space Debris*, vol. 8, Apr. 2021. DOI: [10.13140/RG.2.2.30685.33765](https://doi.org/10.13140/RG.2.2.30685.33765).
- [37] M. Viikinkoski, J. Hanu, M. Kaasalainen, F. Marchis, and J. urech, “Adaptive optics and lightcurve data of asteroids: twenty shape models and information content analysis,” *Astronomy and Astrophysics*, vol. 607, pp. 1–14, Nov. 2017. DOI: [10.1051/0004-6361/201731456](https://doi.org/10.1051/0004-6361/201731456).
- [38] L. Robinson and C. Frueh, “Light curve inversion for reliable shape reconstruction of human-made space objects,” in *Proceedings of the 32nd AIAA/AAS Astrodynamics Specialist Conference*, Sep. 2022, pp. 1–19.

- [39] B. Nicolet, A. Jacobson, and W. Jakob, “Large steps in inverse rendering of geometry,” *ACM Transactions on Graphics (Proceedings of SIGGRAPH Asia)*, vol. 40, no. 6, Dec. 2021. doi: [10.1145/3478513.3480501](https://doi.org/10.1145/3478513.3480501).
- [40] F. L. Markley and J. L. Crassidis, *Fundamentals of Spacecraft Attitude Determination and Control*. Springer, May 2014.
- [41] M. D. Shuster, “Survey of attitude representations,” *Journal of the Astronautical Sciences*, vol. 41, no. 4, pp. 439–517, Oct. 1993.
- [42] H. Krag, “A method for the validation of space debris models and for the analysis and planning of radar and optical surveys,” Ph.D. dissertation, Technische Universität Braunschweig, Mar. 2003.
- [43] D. Newell and E. Tiesinga, *The international system of units (si), 2019 edition*, en, Aug. 2019. doi: <https://doi.org/10.6028/NIST.SP.330-2019>.
- [44] L. T. Sharpe, A. Stockman, W. Jagla, and H. Jägle, “A luminous efficiency function, $V^*(\lambda)$, for daylight adaptation,” *Journal of Vision*, vol. 5, no. 11, pp. 3–3, Dec. 2005, ISSN: 1534-7362. doi: [10.1167/5.11.3](https://doi.org/10.1167/5.11.3). eprint: https://arvojournals.org/arvo/content/_public/journal/jov/932833/jov-5-11-3.pdf. [Online]. Available: <https://doi.org/10.1167/5.11.3>.
- [45] K. A. Pickering, “The Southern Limits of the Ancient Star Catalog and the Commentary of Hipparchos,” *DIO*, vol. 12, pp. 3–27, Sep. 2002.
- [46] F. Falchi, P. Cinzano, D. Duriscoe, *et al.*, *Supplement to: The new world atlas of artificial night sky brightness. v. 1.1. gfz data services*. <https://doi.org/10.5880/GFZ.1.4.2016.001>, Accessed: 2023-08-25, 2016.
- [47] F. Falchi, P. Cinzano, D. Duriscoe, *et al.*, “The new world atlas of artificial night sky brightness,” *Science Advances*, vol. 2, no. 6, e1600377, 2016. doi: [10.1126/sciadv.1600377](https://doi.org/10.1126/sciadv.1600377). eprint: <https://www.science.org/doi/pdf/10.1126/sciadv.1600377>. [Online]. Available: <https://www.science.org/doi/abs/10.1126/sciadv.1600377>.
- [48] F. Patat, O. S. Ugolnikov, and O. V. Postylyakov, “UBVRI twilight sky brightness at ESO-Paranal,” *Astronomy and Astrophysics*, vol. 455, no. 1, pp. 385–393, Aug. 2006. doi: [10.1051/0004-6361:20064992](https://doi.org/10.1051/0004-6361:20064992). arXiv: [astro-ph/0604128 \[astro-ph\]](https://arxiv.org/abs/astro-ph/0604128).

- [49] A. e. a. Vallenari, “Gaia Data Release 3. Summary of the content and survey properties,” *Astronomy & Astrophysics*, vol. 674, A1, A1, Jun. 2023. doi: [10.1051/0004-6361/202243940](https://doi.org/10.1051/0004-6361/202243940). arXiv: [2208.00211 \[astro-ph.GA\]](https://arxiv.org/abs/2208.00211).
- [50] J. C. Segovia, *Astroquery.gaia package*, <https://astroquery.readthedocs.io/en/latest/gaia/gaia.html>, Accessed: 2023-08-21, 2016.
- [51] G. M. Daniels, “A night sky model for satellite search systems.,” *Optical Engineering*, vol. 16, pp. 66–71, Feb. 1977.
- [52] F. E. Roach, “A Photometric Model of the Zodiacal Light,” *Astronomical Journal*, vol. 77, p. 887, Dec. 1972. doi: [10.1086/111363](https://doi.org/10.1086/111363).
- [53] *Wavefront obj file format*, <https://www.loc.gov/preservation/digital/formats/fdd/fdd000507.shtml>, Accessed: 2023-08-30, 2020.
- [54] B. Duvenhage, K. Bouatouch, and D. Kourie, “Numerical verification of bidirectional reflectance distribution functions for physical plausibility,” in *SAICSIT ’13: Proceedings of the South African Institute for Computer Scientists and Information Technologists Conference*, Oct. 2013, pp. 200–208, ISBN: 9781450321129. doi: [10.1145/2513456.2513499](https://doi.org/10.1145/2513456.2513499).
- [55] R. M. Soldado and C. U. Almagro, “An overview of brdf models,” 2012. [Online]. Available: <https://api.semanticscholar.org/CorpusID:44900609>.
- [56] B. T. Phong, “Illumination for computer generated pictures,” in *Seminal Graphics: Pioneering Efforts That Shaped the Field*. New York, NY, USA: Association for Computing Machinery, 1998, pp. 95–101, ISBN: 158113052X. [Online]. Available: [%5Curl%7Bhttps://doi.org/10.1145/280811.280980%7D](https://doi.org/10.1145/280811.280980).
- [57] T. Möller and B. Trumbore, “Fast, minimum storage ray-triangle intersection,” *Journal of Graphics Tools*, vol. 2, Aug. 2005. doi: [10.1145/1198555.1198746](https://doi.org/10.1145/1198555.1198746).
- [58] W. Keeter, *Nasa 3d models*, <https://nasa3d.arc.nasa.gov/models/>, Accessed: 2022-04-27, Feb. 2013.
- [59] H. Kolivand and M. S. Sunar, “Survey of shadow volume algorithms in computer graphics,” *IETE Technical Review*, vol. 30, no. 1, pp. 38–46, 2013. doi: [10.4103/0256-4602.107338](https://doi.org/10.4103/0256-4602.107338).

- [60] S. Brabec, T. Annen, and H.-P. Seidel, “Practical shadow mapping,” *Journal of Graphics Tools*, vol. 7, no. 4, pp. 9–18, 2002.
- [61] R. Santamaria, *Raylib*, <https://www.raylib.com>, Accessed: 2022-04-28, Nov. 2021.
- [62] J. J. Little, “An iterative method for reconstructing convex polyhedra from extended gaussian images,” in *Proceedings of the Third AAAI Conference on Artificial Intelligence*, ser. AAAI’83, Washington, D.C.: AAAI Press, 1983, pp. 247–250.
- [63] H. Minkowski, “Allgemeine lehrsätze über die konvexen polyeder,” in *Ausgewählte Arbeiten zur Zahlentheorie und zur Geometrie: Mit D. Hilberts Gedächtnisrede auf H. Minkowski, Göttingen 1909*. Springer Vienna, 1909, ch. 22, pp. 121–139. [Online]. Available: https://doi.org/10.1007/978-3-7091-9536-9_5.
- [64] J. J. Little, “Extended gaussian images, mixed volumes, shape reconstruction,” in *Proceedings of the First Annual Symposium on Computational Geometry*, ser. SCG ’85, Baltimore, Maryland, USA: Association for Computing Machinery, 1985, pp. 15–23, ISBN: 0897911636. DOI: [10.1145/323233.323236](https://doi.org/10.1145/323233.323236). [Online]. Available: <https://doi.org/10.1145/323233.323236>.
- [65] B. Keinert, M. Innmann, M. Sänger, and M. Stamminger, “Spherical fibonacci mapping,” *ACM Transactions on Graphics*, vol. 34, no. 6, pp. 1–7, 2015.
- [66] E. W. Weisstein, *Sphere point picking*, <https://mathworld.wolfram.com/SpherePointPicking.html>, Accessed: 2022-07-03, 2002.
- [67] C. L. Lawson and R. J. Hanson, “Solving least squares problems,” in *Classics in applied mathematics*, 1976. [Online]. Available: <https://api.semanticscholar.org/CorpusID:122862057>.
- [68] R. Bro and S. De Jong, “A fast non-negativity-constrained least squares algorithm,” *Journal of Chemometrics*, vol. 11, no. 5, pp. 393–401, 1997. DOI: [https://doi.org/10.1002/\(SICI\)1099-128X\(199709/10\)11:5<393::AID-CEM483>3.0.CO;2-L](https://doi.org/10.1002/(SICI)1099-128X(199709/10)11:5<393::AID-CEM483>3.0.CO;2-L). [Online]. Available: <https://onlinelibrary.wiley.com/doi/abs/10.1002/%28SICI%291099-128X%28199709/10%2911%3A5%3C393%3A%3AAID-CEM483%3E3.0.CO%3B2-L>.
- [69] C. T. Loop, “Smooth subdivision surfaces based on triangles,” Ph.D. dissertation, University of Utah, Aug. 1987. [Online]. Available: <https://www.microsoft.com/en-us/research/publication/smooth-subdivision-surfaces-based-on-triangles/>.